

Physics-Information-Aided Kriging: Constructing Covariance Functions using Stochastic Simulation Models

Xiu Yang^{*1}, Guzel D. Tartakovsky², and Alexandre M. Tartakovsky³

¹Department of Industrial and Systems Engineering, Lehigh University, Bethlehem, PA 18015

²Intera

³Civil and Environmental Engineering, University of Illinois, Urbana-Champaign, IL 61801 and Pacific Northwest National Laboratory, Richland, WA 99354

November 17, 2021

Abstract

In this work, we propose a new Gaussian process regression (GPR) method: physics information aided Kriging (PhIK). In the standard data-driven Kriging, the unknown function of interest is usually treated as a Gaussian process with assumed stationary covariance with hyperparameters estimated from data. In PhIK, we compute the mean and covariance function from realizations of available stochastic models, e.g., from realizations of governing stochastic partial differential equations solutions. Such constructed Gaussian process generally is non-stationary, and does not assume a specific form of the covariance function. Our approach avoids the optimization step in data-driven GPR methods to identify the hyperparameters. More importantly, we prove that the physical constraints in the form of a deterministic linear operator are guaranteed in the resulting prediction. We also provide an error estimate in preserving the physical constraints when errors are included in the stochastic model realizations. To reduce the computational cost of obtaining stochastic model realizations, we propose a multilevel Monte Carlo estimate of the mean and covariance functions. Further, we present an active learning algorithm that guides the selection of additional observation locations. The efficiency and accuracy of PhIK are demonstrated for reconstructing a partially known modified Branin function, studying a three-dimensional heat transfer problem and learning a conservative tracer distribution from sparse concentration measurements.

Keywords: physics-informed, Gaussian process regression, active learning, error bound.

1 Introduction

Gaussian process regression (GPR), also known as *Kriging* in geostatistics, is a widely used method in applied mathematics, statistics and machine learning for constructing surrogate models, interpolation, classification, supervised learning, and active learning [19, 54, 56]. GPR constructs a statistical model of a partially observed function (of time and/or space) assuming this function is a realization of a Gaussian process (GP). GP is uniquely described by its mean and covariance function. In the standard (here referred to as *data-driven*) GP, prescribed forms of mean and covariance functions are assumed, and the hyperparameters (e.g., variance and correlation length) are computed from data via negative log-marginal likelihood function minimization. There are several variants of GPR, including simple, ordinary, and universal Kriging [29]. GPR is also closely related to kernel machines in machine learning, but it includes more information as it provides the uncertainty estimate [61].

*Email: xiy518@lehigh.edu

In the ordinary Kriging, a constant mean and a prescribed form of the stationary covariance function (also known as *kernel*) are used. This stationarity assumption reduces the number of hyperparameters and model complexity. However, in many practical problems, state variables are not stationary. Hence, using a stationary GP may not yield accurate approximation. Furthermore, even if the state variable is stationary, there are many choices of the covariance functions with different smoothness properties [16, 15].

In addition to (measurement) data, physical models that reflect (partial) understanding of the underlying system are available in many areas. Especially, when obtaining measurements or conducting experiments is very costly, which is quite common in practical problems, these physical models and simulation tools are critical in research and applications. For example, in hydrology study, partial physical knowledge is available in the form of partial differential equations (e.g., the Darcy law governing the hydraulic head) with unknown boundary, initial condition, and/or space-dependent coefficient (e.g., the hydraulic conductivity). Subsequently, the standard treatment is to model the unknown parameters as random variables/fields to formulate stochastic partial differential equations (SPDEs). In general, the covariance of the state variable of SPDEs defined on a bounded domain with non-periodic boundary conditions is non-stationary [57, 26]. This non-stationarity can help reflecting inhomogeneity of the state variables in the underlying physical system. Some success has been shown to incorporate physical knowledge in kernels, e.g., [55, 50, 38] computed kernels for linear and weakly nonlinear (allowing accurate linearization) ordinary and partial differential equations by substituting a GPR approximation of the state variables in governing equations and obtaining a likelihood to be solved by optimization methods. However, for more complex systems, such as those involving strongly nonlinear terms and random variables/fields, it can be difficult to implement GPR in this manner in that the GP representing the system is no longer Gaussian after a nonlinear mapping.

In this work, we propose to incorporate physical knowledge in Kriging by computing mean and covariance function from a physics model. Therefore, we call this method the *physics-information-aided Kriging*, or *PhIK*. Specifically, we compute the mean and covariance function used in Kriging from simulation ensembles. Because computational tools, including commercial and open source packages, have achieved a significant degree of maturity for many science applications (e.g., climate modeling, hydrology, aerospace engineering, electrical engineering, etc.), we can run parallel simulations in the “Monte Carlo (MC) mode” efficiently. This could be achieved by treating unknown parameters as random parameters or random fields. This is a common step in uncertainty quantification (UQ) and sensitivity analysis [35, 63, 25, 66, 75, 12], and existing data from these research can be reused in the proposed method. We will show in this work that using empirical mean and covariance from these MC (or other sampling techniques) simulations to construct a GP (i.e., to estimate the mean and covariance function) helps integrating physical knowledge in the resulting model. In addition to making GPR prediction more accurate in terms of preserving some physical constraints, this approach removes the need for assuming a specific form of the kernel and solving an optimization problem for its hyperparameters. A similar idea is adopted in the ensemble Kalman filter (EnKF) [18] for data assimilation in time-dependent problems, where the ensemble mean and variance are used.

The cost of estimating mean and covariance depends on the size and complexity of the physical model. We propose to reduce this cost by using multilevel Monte Carlo (MLMC) [22]. Traditionally, MLMC has been used to approximate the mean and one-point moments by combining a relatively few high-resolution simulations with a (larger) number of coarse resolution simulations to compute moments with the desired accuracy. We extend MLMC for approximating covariance function, a two-point second moment. Then, we provide error estimates for PhIK and MLMC-based PhIK describing how well physics constraints are preserved. Finally, we apply PhIK for active learning (i.e., choosing additional measurement locations) using the posterior variance in the PhIK method.

This work is organized as follows: Section 2 introduces PhIK, the MLMC method for estimating statistics, the error estimates for PhIK, and active learning. Section 3 provides two numerical examples to demonstrate the efficiency of the proposed method. Conclusions are presented in Section 4.

2 Methodology

This section begins by reviewing the general GPR framework [19] and the Kriging method based on the assumption of stationary GP [2]. Next, we introduce the PhIK and MLMC-based PhIK. Finally, we present an active learning algorithm based on PhIK.

2.1 GPR framework

We denote the observation locations as $\mathbf{X} = \{\mathbf{x}^{(i)}\}_{i=1}^N$ ($\mathbf{x}^{(i)}$ are d -dimensional vectors in $D \subseteq \mathbb{R}^d$) and the observed state values at these locations as $\mathbf{y} = (y^{(1)}, y^{(2)}, \dots, y^{(N)})^\top$ ($y^{(i)} \in \mathbb{R}$). For simplicity, we assume that $y^{(i)}$ are scalars. We aim to predict y at any new location $\mathbf{x}^* \in D$. The GPR method treats the observed data as a realization of random field $Y : D \times \Omega \rightarrow \mathbb{R}$:

$$Y(\mathbf{x}; \omega) \sim \mathcal{GP}(\mu(\mathbf{x}), k(\mathbf{x}, \mathbf{x}')), \quad (1)$$

where and $k : D \times D \rightarrow \mathbb{R}$ are the mean and covariance (kernel) functions:

$$\mu(\mathbf{x}) = \mathbb{E}\{Y(\mathbf{x})\} \quad (2)$$

$$k(\mathbf{x}, \mathbf{x}') = \text{Cov}\{Y(\mathbf{x}), Y(\mathbf{x}')\} = \mathbb{E}\{(Y(\mathbf{x}) - \mu(\mathbf{x}))(Y(\mathbf{x}') - \mu(\mathbf{x}'))\}, \quad (3)$$

and $Y(\mathbf{x})$ is the concise notation of $Y(\mathbf{x}; \omega)$. The variance of $Y(\mathbf{x})$ is $k(\mathbf{x}, \mathbf{x})$, and its standard deviation is $\sigma(\mathbf{x}) = \sqrt{k(\mathbf{x}, \mathbf{x})}$.

In practice, one can parametrize forms of $\mu(\mathbf{x})$ and $k(\mathbf{x}, \mathbf{x})$. For example, in the widely used ordinary Kriging method, a stationary GP is assumed. In this case, μ is set as a constant $\mu(\mathbf{x}) \equiv \mu$. More importantly, it is assumed that $k(\mathbf{x}, \mathbf{x}') = k(\boldsymbol{\tau})$, where $\boldsymbol{\tau} = \mathbf{x} - \mathbf{x}'$, and $\sigma^2(\mathbf{x}) = k(\mathbf{x}, \mathbf{x}) = k(\mathbf{0}) = \sigma^2$ is a constant. Popular forms of kernels include polynomial, exponential, Gaussian, and Matérn functions. For example, the Gaussian kernel can be written as $k(\boldsymbol{\tau}) = \sigma^2 \exp(-\frac{1}{2}\|\boldsymbol{\tau}\|_w^2)$, where the weighted norm is defined as

$\|\boldsymbol{\tau}\|_w^2 = \sum_{i=1}^d \left(\frac{\tau_i - \tau'_i}{l_i}\right)^2$ and l_i 's are correlation lengths. Taking a classical frequentist stance, we have

the following best linear unbiased predictor (BLUP) [54, 27]

$$\hat{y}(\mathbf{x}^*) = \hat{\mu} + \mathbf{c}^\top \mathbf{C}^{-1}(\mathbf{y} - \hat{\mu}\mathbf{1}), \quad (4)$$

and its mean squared error

$$\hat{s}^2(\mathbf{x}^*) = \hat{\sigma}^2 - \mathbf{c}^\top \mathbf{C}^{-1} \mathbf{c} + \frac{(1 - \mathbf{1}^\top \mathbf{C}^{-1} \mathbf{c})^2}{\mathbf{1}^\top \mathbf{C}^{-1} \mathbf{1}}, \quad (5)$$

where \mathbf{C} is the following covariance matrix:

$$\mathbf{C} = \begin{pmatrix} k(\mathbf{x}^{(1)}, \mathbf{x}^{(1)}) & \dots & k(\mathbf{x}^{(1)}, \mathbf{x}^{(N)}) \\ \vdots & \ddots & \vdots \\ k(\mathbf{x}^{(N)}, \mathbf{x}^{(1)}) & \dots & k(\mathbf{x}^{(N)}, \mathbf{x}^{(N)}) \end{pmatrix}, \quad (6)$$

and $\mathbf{c} = (k(\mathbf{x}^{(1)}, \mathbf{x}^*), \dots, k(\mathbf{x}^{(N)}, \mathbf{x}^*))^\top$, $\mathbf{1} = (1, 1, \dots, 1)^\top$, $\hat{\mu} = \frac{\mathbf{1}^\top \mathbf{C}^{-1} \mathbf{c}}{\mathbf{1}^\top \mathbf{C}^{-1} \mathbf{1}}$. Hyperparameters $\hat{\sigma}$ and \hat{l}_i can be obtained by maximum likelihood estimate. Of note, in most literature, Eqs. (4) and (5) are based on correlation function and matrix. Here, we use covariance function and matrix in the expressions (which is more general) to keep consistency with PhIK description, which does not assume $Y(\mathbf{x}; \omega)$ is stationary.

Alternatively, given complete information of the prior GPR $Y(\mathbf{x})$ (i.e., $\mu(\mathbf{x})$ and $k(\mathbf{x}, \mathbf{x})$ are given), a Bayesian approach uses the posterior distribution $Y(\mathbf{x}^*) | \mathbf{X}, \mathbf{y} \sim \mathcal{N}(\hat{y}(\mathbf{x}^*), \hat{s}^2(\mathbf{x}^*))$ for the prediction [11, 51], where

$$\hat{y}(\mathbf{x}^*) = \mu(\mathbf{x}^*) + \mathbf{c}^\top \mathbf{C}^{-1}(\mathbf{y} - \mu), \quad (7)$$

$$\hat{s}^2(\mathbf{x}^*) = \sigma^2(\mathbf{x}^*) - \mathbf{c}^\top \mathbf{C}^{-1} \mathbf{c}, \quad (8)$$

and $\boldsymbol{\mu} = (\mu(\mathbf{x}^{(1)}), \dots, \mu(\mathbf{x}^{(N)}))^\top$.

Moreover, to account for the observation noise, one can assume that the noise is independent and identically distributed (i.i.d.) Gaussian random variables with zero mean and variance δ^2 , and replace \mathbf{C} with $\mathbf{C} + \delta^2\mathbf{I}$, which, from the Bayesian perspective, results in a posterior distribution of the normal random $Y(\mathbf{x}^*)$. Moreover, in the noiseless case, if \mathbf{C} is not invertible, following the common GPR approach, one can add a small regularization term $\alpha\mathbf{I}$ (α is a small positive real number) to \mathbf{C} such that it becomes full rank. Adding the regularization term is equivalent to assuming there is a measurement noise.

A more general approach is to assume a non-stationary covariance function, which potentially increases the number of hyperparameters [40, 45, 7]. However, these methods still need to assume a specific form of the correlation functions according to experience. The key computational challenge in the data-driven GPR is the optimization step of maximizing the (marginal) likelihood. In many practical cases, this is a non-convex optimization problem, and the condition number of \mathbf{C} can be quite large. A more fundamental challenge in the data-driven GPR is that it does not explicitly account for physical constraints and requires a large amount of data to accurately model the physics. The PhIK introduced in the next section aims to address both of these challenges.

2.2 PhIK

We design PhIK based on the Bayesian interpretation of the GPR method. Namely, we specify a prior distribution of $Y(\mathbf{x})$, which is achieved by taking advantage of the existing domain knowledge in the form of realizations of a stochastic model of the underlying system. As such, there is no need to assume a specific form of the correlation functions and solve an optimization problem for the hyperparameters. This idea is motivated by many scientific and engineering problems, where numerical or analytical physics-based models are available. These models typically include random parameters or random processes/fields to reflect the lack of understanding (e.g., physical laws) or information (e.g., coefficients, parameters, etc.) of the real system. Then, MC type of simulations are conducted to generate an ensemble of state variables, from which the statistics of these state variables, e.g., mean and standard deviation, are estimated. We can compute the empirical mean and covariance of the ensemble, and use them to construct a GP. Finally, the results of PhIK is this GP conditioned on the observed state variables.

Specifically, assume that we have M realizations, denoted as $\{Y^m(\mathbf{x})\}_{m=1}^M (\mathbf{x} \in D)$, of a stochastic model $u : D \times \Omega \rightarrow \mathbb{R}$. The empirical mean of these realizations is

$$\mu_{MC}(\mathbf{x}) = \frac{1}{M} \sum_{m=1}^M Y^m(\mathbf{x}), \mu_{MC}(\mathbf{x}) = \frac{1}{M} \sum_{m=1}^M Y^m(\mathbf{x}), \quad (9)$$

and the empirical covariance is

$$k_{MC}(\mathbf{x}, \mathbf{x}') = \frac{1}{M-1} \sum_{m=1}^M (Y^m(\mathbf{x}) - \mu_{MC}(\mathbf{x})) (Y^m(\mathbf{x}') - \mu_{MC}(\mathbf{x}')). \quad (10)$$

It is clear that $\mu_{MC}(\mathbf{x})$ and $k_{MC}(\mathbf{x}, \mathbf{x}')$ are unbiased estimates of $\mathbb{E}\{u(\mathbf{x})\}$ and $\text{Cov}\{u(\mathbf{x}), u(\mathbf{x}')\}$, respectively. Also, the covariance matrix of \mathbf{C} in Eq. (6) has the following empirical counterpart:

$$\mathbf{C}_{MC} = \frac{1}{M-1} \sum_{m=1}^M (\mathbf{Y}^m - \boldsymbol{\mu}_{MC})(\mathbf{Y}^m - \boldsymbol{\mu}_{MC})^\top, \quad (11)$$

where $\mathbf{Y}^m = (Y^m(\mathbf{x}^{(1)}), \dots, Y^m(\mathbf{x}^{(N)}))^\top$, $\boldsymbol{\mu}_{MC} = (\mu_{MC}(\mathbf{x}^{(1)}), \dots, \mu_{MC}(\mathbf{x}^{(N)}))^\top$. Similar to the standard GPR, PhIK results in a posterior distribution at location \mathbf{x}^* as $Y(\mathbf{x}^*)|\mathbf{X}, \mathbf{y}, \alpha \sim \mathcal{N}(\hat{y}(\mathbf{x}^*), \hat{s}^2(\mathbf{x}^*))$, where

$$\hat{y}(\mathbf{x}^*) = \mu_{MC}(\mathbf{x}^*) + \mathbf{c}_{MC}^\top (\mathbf{C}_{MC} + \alpha\mathbf{I})^{-1} (\mathbf{y} - \boldsymbol{\mu}_{MC}), \quad (12)$$

$$\hat{s}^2(\mathbf{x}^*) = \hat{\sigma}_{MC}^2(\mathbf{x}^*) - \mathbf{c}_{MC}^\top (\mathbf{C}_{MC} + \alpha\mathbf{I})^{-1} \mathbf{c}_{MC}, \quad (13)$$

where $\hat{\sigma}_{MC}^2(\mathbf{x}^*) = k_{MC}(\mathbf{x}^*, \mathbf{x}^*)$ is the variance of data set $\{Y^m(\mathbf{x}^*)\}_{m=1}^M$, $\mathbf{c}_{MC} = (k_{MC}(\mathbf{x}^{(1)}, \mathbf{x}^*), \dots, k_{MC}(\mathbf{x}^{(N)}, \mathbf{x}^*))$, and $\alpha\mathbf{I}$ is the regularization term because \mathbf{C}_{MC} is not full rank. By construction, PhIK can be considered as a Kriging method using empirical statistics. More importantly, PhIK has several advantages:

- It does not need to assume stationarity of the GP.
- It does not need to assume a specific form of the covariance relation. Thus, the form of the resulting GP is more flexible.
- It does not need to solve the optimization problem to identify hyperparameters, which can be a challenging problem often suffering from the ill-conditioned covariance matrix.
- It incorporates physical constraints via the mean and covariance function.

Next, we present a theorem that details how well PhIK prediction preserves linear physical constraints. In this analysis, we treat the stochastic model $u(\mathbf{x}; \omega)$ as a random field.

Theorem 2.1. *Consider random fields $u(\mathbf{x}; \omega) : \mathbb{R}^d \times \Omega \rightarrow \mathbb{R}$ and $g(\mathbf{x}; \omega) : \mathbb{R}^{d'} \times \Omega \rightarrow \mathbb{R}$, where d and d' are positive integers. Each realization of $u(\mathbf{x}; \omega)$ is in a normed space $(U, \|\cdot\|_U)$ and each realization of $g(\mathbf{x}; \omega)$ is in a normed space $(V, \|\cdot\|_V)$. Assume that $\mathcal{L} : (U, \|\cdot\|_U) \rightarrow (V, \|\cdot\|_V)$ is a linear operator such that $\|\mathcal{L}u(\mathbf{x}; \omega) - g(\mathbf{x}; \omega)\| \leq \epsilon$ for any $\omega \in \Omega$. Let $\{Y^m(\mathbf{x})\}_{m=1}^M$ be a finite number of realizations of $u(\mathbf{x}; \omega)$, i.e., $Y^m(\mathbf{x}) = u(\mathbf{x}; \omega^m)$. Then, the prediction $\hat{y}(\mathbf{x})$ from PhIK satisfies*

$$\|\mathcal{L}\hat{y}(\mathbf{x}) - \overline{g(\mathbf{x})}\|_V \leq \epsilon + \left[2\epsilon \sqrt{\frac{M}{M-1}} + \sigma(g(\mathbf{x}; \omega^m)) \right] \cdot \left\| (\mathbf{C} + \alpha\mathbf{I})_{MC}^{-1} (\mathbf{y} - \boldsymbol{\mu}_{MC}) \right\|_{\infty} \sum_{i=1}^N \sigma(Y^m(\mathbf{x}^{(i)})), \quad (14)$$

where $\sigma(Y^m(\mathbf{x}^{(i)}))$ is the standard deviation of the data set $\{Y^m(\mathbf{x}^{(i)})\}_{m=1}^M$ for each fixed $\mathbf{x}^{(i)}$, $\overline{g(\mathbf{x})} = \frac{1}{M} \sum_{m=1}^M g(\mathbf{x}; \omega^m)$, and $\sigma(g(\mathbf{x}; \omega^m)) = \left(\frac{1}{M-1} \sum_{m=1}^M \|g(\mathbf{x}; \omega^m) - \overline{g(\mathbf{x})}\|_V^2 \right)^{\frac{1}{2}}$.

We present the proof of this theorem in Appendix A. In the following discussion, we rewrite $\|\cdot\|_V$ as $\|\cdot\|$ to simplify the notation.

This theorem holds for various norms, e.g., L_2 norm, L_{∞} norm, and H^1 norm. In practice, the realizations $Y^m(\mathbf{x})$ are obtained by numerical simulations and are subject to numerical errors, model errors, etc. Thus, the theorem includes ϵ in the upper bound. It also indicates that the standard deviation of ensemble member Y^m at all observation locations $\mathbf{x}^{(i)}$ affects the upper bound of $\|\mathcal{L}(\hat{y}(\mathbf{x}) - \overline{g(\mathbf{x})})\|$. If the variance of $Y^m(\mathbf{x}^{(i)})$ is small at every $\mathbf{x}^{(i)}$, e.g., when the physical model is less uncertain, the resulting prediction $\hat{y}(\mathbf{x})$ will not violate the linear constraint much, i.e., $\|\mathcal{L}\hat{y}(\mathbf{x}) - \overline{g(\mathbf{x})}\|$ is small. Moreover, if $g(\mathbf{x}; \omega)$ is a deterministic function $g(\mathbf{x})$, then $\sigma(g(\mathbf{x}; \omega^m)) = 0$ in the upper bound (see Eq. (14)). Another important factor for the error bound is $\max_i |\tilde{\alpha}_i|$, i.e., $\|(\mathbf{C} + \alpha\mathbf{I})_{MC}^{-1} (\mathbf{y} - \boldsymbol{\mu}_{MC})\|_{\infty}$. Because $\|(\mathbf{C}_{MC} + \alpha\mathbf{I})^{-1} (\mathbf{y} - \boldsymbol{\mu}_{MC})\|_{\infty} \leq \|(\mathbf{C}_{MC} + \alpha\mathbf{I})^{-1} (\mathbf{y} - \boldsymbol{\mu}_{MC})\|_2 \leq \|(\mathbf{C}_{MC} + \alpha\mathbf{I})^{-1}\|_2 \|\mathbf{y} - \boldsymbol{\mu}_{MC}\|_2$, the upper bound can be affected by the difference between the physical model output and the observation, i.e., $\|\mathbf{y} - \boldsymbol{\mu}_{MC}\|_2$, which is affected by the physical model's accuracy, and the reciprocal of the smallest eigenvalue of $\mathbf{C}_{MC} + \alpha\mathbf{I}$, which is bounded by α^{-1} . In addition, the following corollary describes a special case.

Corollary 2.2. *In Theorem 2.1, if g is a deterministic function, i.e., $g(\mathbf{x}; \omega) = g(\mathbf{x})$, and $\mathcal{L}u(\mathbf{x}; \omega) = g(\mathbf{x})$ for any $\omega \in \Omega$, then $\mathcal{L}\hat{y}(\mathbf{x}) = g(\mathbf{x})$.*

Proof. Because $\mathcal{L}Y^m(\mathbf{x}) = g(\mathbf{x})$ and $\mathcal{L}\boldsymbol{\mu}_{MC}(\mathbf{x}) = \overline{g(\mathbf{x})} = g(\mathbf{x})$, we have

$$\begin{aligned} \mathcal{L}k_{MC}(\mathbf{x}, \mathbf{x}^{(i)}) &= \mathcal{L} \left[\frac{1}{M-1} \sum_{m=1}^M \left(Y^m(\mathbf{x}) - \boldsymbol{\mu}_{MC}(\mathbf{x}) \right) \left(Y^m(\mathbf{x}^{(i)}) - \boldsymbol{\mu}_{MC}(\mathbf{x}^{(i)}) \right) \right] \\ &= \frac{1}{M-1} \sum_{m=1}^M \mathcal{L} \left(Y^m(\mathbf{x}) - \boldsymbol{\mu}_{MC}(\mathbf{x}) \right) \left(Y^m(\mathbf{x}^{(i)}) - \boldsymbol{\mu}_{MC}(\mathbf{x}^{(i)}) \right) = 0. \end{aligned}$$

Therefore,

$$\mathcal{L}\hat{y}(\mathbf{x}) = \mathcal{L}\left(\mu_{MC}(\mathbf{x}) + \sum_{i=1}^N \tilde{a}_i k_{MC}(\mathbf{x}, \mathbf{x}^{(i)})\right) = \mathcal{L}\mu_{MC}(\mathbf{x}) = g(\mathbf{x}).$$

□

For example, if $u(\mathbf{x};\omega)$ satisfies the Dirichlet boundary condition $u(\mathbf{x};\omega) = g(\mathbf{x})$, $\mathbf{x} \in \partial D_D$ for any $\omega \in \Omega$, then $\hat{y}(\mathbf{x}) = g(\mathbf{x})$, $\mathbf{x} \in \partial D_D$. Similarly, if $u(\mathbf{x};\omega)$ satisfies the Neumann boundary condition, $\partial u(\mathbf{x};\omega)/\partial \mathbf{n} = 0$, $\mathbf{x} \in \partial D_N$, then $\partial \hat{y}(\mathbf{x};\omega)/\partial \mathbf{n} = 0$, $\mathbf{x} \in \partial D_N$. Another example is if u satisfies $\nabla \cdot u(\mathbf{x};\omega) = 0$ for any $\omega \in \Omega$, $\hat{y}(\mathbf{x})$ is also a divergence-free field. In general cases, i.e., g is random and $\epsilon \neq 0$, the upper bound in Theorem 2.1 describes how well a physical constraint is preserved.

In this work, we choose to use the MC method to compute the mean and covariance because of its robustness. Here, the criteria for choosing M are similar to the standard MC method. In our numerical examples, the size of M is around 100 for demonstration purpose. When the system's number of degrees of freedom (DOF) is large (e.g., a high-resolution 3D model), the cost of estimating the mean and covariance using MC method can be very high. Several methods can be used to reduce the cost of estimating empirical statistics, including quasi-Monte Carlo [37], probabilistic collocation [65], Analysis Of Variance (ANOVA) [68], and compressive sensing [69], as well as mode reduction methods, e.g., the moment equation method [58]. Depending on the applications, these methods could be significantly more efficient than MC, and some of them have been implemented in studying uncertainty and sensitivity of complex systems such as climate [46], hydrology [25], and urban flow [33]. It is not difficult to show that conclusions similar to Theorem 2.1 hold if $\mu(\mathbf{x})$ and $k(\mathbf{x}, \mathbf{x}')$ are approximated using a *linear combination* of $\{Y^m(\mathbf{x})\}_{m=1}^M$, where these realizations are based on a different sampling strategy.

2.3 Estimating statistics using MLMC

The MC method requires a sufficiently large ensemble of Y to accurately estimate the mean and covariance matrix, which, in some applications, can be unpractical. To address this issue, instead of using aforementioned different sampling strategies, we estimate empirical statistics using MLMC. For simplicity, we demonstrate the idea via two-level MLMC simulations. We use $Y_L^m(\mathbf{x})$ ($m = 1, \dots, M_L$) and $Y_H^m(\mathbf{x})$ ($m = 1, \dots, M_H$) to denote M_L low-accuracy and M_H high-accuracy realizations of the stochastic model for the system. We assume that Y_L^m and Y_H^m are realizations of stochastic models $u_L : D_L \times \Omega \rightarrow \mathbb{R}$ and $u_H : D_H \times \Omega \rightarrow \mathbb{R}$, respectively. We also denote $\bar{u}(\mathbf{x}) = u_H(\mathbf{x}) - u_L(\mathbf{x})$. For example, $D_L \subset \mathbb{R}^d$ and $D_H = D \subseteq \mathbb{R}^d$ can be coarse and fine grids in numerical simulations, respectively. Thus, u_L and u_H are low- and high-resolution random processes. In this case, when computing \bar{u} , we interpolate u_L from D_L to D_H . To simplify notations, we use u_L to denote both the low-resolution random process on D_L and the interpolated random process from D_L to D_H in the MLMC formula. The mean of $u_H(\mathbf{x})$ is estimated as

$$\mathbb{E}\{u_H(\mathbf{x})\} \approx \mu_{MLMC}(\mathbf{x}) = \frac{1}{M_L} \sum_{m=1}^{M_L} Y_L^m(\mathbf{x}) + \frac{1}{M_H} \sum_{m=1}^{M_H} \bar{Y}^m(\mathbf{x}), \quad (15)$$

which is the standard MLMC estimate of the mean [22]. In the past, MLMC was used only to estimate single point statistics, e.g., [3, 5, 6]. Here, we propose an MLMC estimate of the covariance function of $u_H(\mathbf{x})$ based on the following relationship:

$$\begin{aligned} \text{Cov}\{u_H(\mathbf{x}), u_H(\mathbf{x}')\} &= \text{Cov}\{u_L(\mathbf{x}) + \bar{u}(\mathbf{x}), u_L(\mathbf{x}') + \bar{u}(\mathbf{x}')\} \\ &= \text{Cov}\{u_L(\mathbf{x}), u_L(\mathbf{x}')\} + \text{Cov}\{u_L(\mathbf{x}), \bar{u}(\mathbf{x}')\} \\ &\quad + \text{Cov}\{\bar{u}(\mathbf{x}), u_L(\mathbf{x}')\} + \text{Cov}\{\bar{u}(\mathbf{x}), \bar{u}(\mathbf{x}')\}. \end{aligned} \quad (16)$$

Because u_L and \bar{u} are sampled independently in MLMC, we have

$$\text{Cov}\{u_L(\mathbf{x}), \bar{u}(\mathbf{x}')\} = \text{Cov}\{\bar{u}(\mathbf{x}), u_L(\mathbf{x}')\} = 0.$$

Thus,

$$\text{Cov}\{u_H(\mathbf{x}), u_H(\mathbf{x}')\} = \text{Cov}\{u_L(\mathbf{x}), u_L(\mathbf{x}')\} + \text{Cov}\{\bar{u}(\mathbf{x}), \bar{u}(\mathbf{x}')\}, \quad (17)$$

and the unbiased MLMC approximation of the covariance is

$$\begin{aligned} & \text{Cov}\{u_H(\mathbf{x}), u_H(\mathbf{x}')\} \approx k_{MLMC}(\mathbf{x}, \mathbf{x}') \\ &= \frac{1}{M_L - 1} \sum_{m=1}^{M_L} \left(Y_L^m(\mathbf{x}) - \frac{1}{M_L} \sum_{m=1}^{M_L} Y_L^m(\mathbf{x}) \right) \left(Y_L^m(\mathbf{x}') - \frac{1}{M_L} \sum_{m=1}^{M_L} Y_L^m(\mathbf{x}') \right) \\ &+ \frac{1}{M_H - 1} \sum_{m=1}^{M_H} \left(\bar{Y}^m(\mathbf{x}) - \frac{1}{M_H} \sum_{m=1}^{M_H} \bar{Y}^m(\mathbf{x}) \right) \left(\bar{Y}^m(\mathbf{x}') - \frac{1}{M_H} \sum_{m=1}^{M_H} \bar{Y}^m(\mathbf{x}') \right). \end{aligned} \quad (18)$$

Finally, the MLMC-based PhIK model yields similar results as MC-based PhIK by replacing all ‘‘MC’’ terms with ‘‘MLMC’’ terms:

$$\hat{y}(\mathbf{x}^*) = \mu_{MLMC}(\mathbf{x}^*) + \mathbf{c}_{MLMC}^\top (\mathbf{C}_{MLMC} + \alpha \mathbf{I})^{-1} (\mathbf{y} - \boldsymbol{\mu}_{MLMC}), \quad (19)$$

$$\hat{s}^2(\mathbf{x}^*) = \sigma_{MLMC}^2(\mathbf{x}^*) - \mathbf{c}_{MLMC}^\top (\mathbf{C}_{MLMC} + \alpha \mathbf{I})^{-1} \mathbf{c}_{MLMC}, \quad (20)$$

where $(\boldsymbol{\mu}_{MLMC})_i = \mu_{MLMC}(\mathbf{x}^{(i)})$, $(\mathbf{c}_{MLMC})_i = k_{MLMC}(\mathbf{x}^{(i)}, \mathbf{x}^*)$, and $(\mathbf{C}_{MLMC})_{ij} = k_{MLMC}(\mathbf{x}^{(i)}, \mathbf{x}^{(j)})$.

The following corollary is a straightforward extension of Theorem 2.1 for PhIK with the mean and covariance obtained from MLMC.

Corollary 2.3. *Assume that $u_H(\mathbf{x}; \omega)$ and $u_L(\mathbf{x}; \omega)$ are random fields defined on $\mathbb{R}^d \times \Omega$ such that each realization of them is in a normed space $(U, \|\cdot\|_U)$. Let $\{Y_H^m(\mathbf{x})\}_{m=1}^{M_H}$ and $\{Y_L^m(\mathbf{x})\}_{m=1}^{M_L}$ be finite ensembles of realizations of $u_H(\mathbf{x}; \omega)$ and $u_L(\mathbf{x}; \omega)$, respectively. $\|\mathcal{L}u_H(\mathbf{x}; \omega) - g(\mathbf{x}; \omega)\| < \epsilon_H$ and $\|\mathcal{L}u_L(\mathbf{x}; \omega) - g(\mathbf{x}; \omega)\| < \epsilon_L$ for any $\omega \in \Omega$, where \mathcal{L} , $\|\cdot\|$ and $g(\mathbf{x}; \omega)$ are defined in Theorem 2.1. The MLMC-based PhIK prediction $\hat{y}(\mathbf{x})$ satisfies*

$$\|\mathcal{L}\hat{y}(\mathbf{x}) - \overline{g(\mathbf{x})}\| \leq C_H \epsilon_H + C_L \epsilon_L + \sigma(g(\mathbf{x}; \omega^m)) \sum_{i=1}^N \tilde{a}_i \sigma(Y_L^m(\mathbf{x}^{(i)})), \quad (21)$$

where $\overline{g(\mathbf{x})}$ is defined in Theorem 2.1,

$$\begin{aligned} C_H &= 1 + 2 \sum_{i=1}^N \tilde{a}_i \sqrt{\frac{M_H}{M_H - 1}} \sigma(\bar{Y}^m(\mathbf{x}^{(i)})), \\ C_L &= 2 + 2 \sum_{i=1}^N \tilde{a}_i \left(\sqrt{\frac{M_L}{M_L - 1}} \sigma(Y_L^m(\mathbf{x}^{(i)})) + \sqrt{\frac{M_H}{M_H - 1}} \sigma(\bar{Y}^m(\mathbf{x}^{(i)})) \right), \end{aligned}$$

and \tilde{a}_i is the i -th entry of $(\mathbf{C}_{MLMC} + \alpha \mathbf{I})^{-1} (\mathbf{y} - \boldsymbol{\mu}_{MLMC})$. Here, $\sigma(g(\mathbf{x}; \omega^m))$ is defined in Theorem 2.1, $\sigma(Y_L^m(\mathbf{x}^{(i)}))$ and $\sigma(\bar{Y}^m(\mathbf{x}^{(i)}))$ are standard deviation of data sets $\{Y_L^m(\mathbf{x}^{(i)})\}_{m=1}^{M_L}$ and $\{\bar{Y}^m(\mathbf{x}^{(i)})\}_{m=1}^{M_H}$, respectively.

We present the proof in Appendix B.

It is not complicated to extend the two-level MC to a general L -level MLMC. We present the following theorem for the L -level ($L > 2$) MLMC-based PhIK error bounds. The proof of this theorem immediately follows from Theorem 2.1.

Theorem 2.4. *Assume that $\{Y_l^m(\mathbf{x})\}_{m=1}^{M_l}$, $l = 1, \dots, L$ are finite ensembles of realizations of random fields $u_l(\mathbf{x}; \omega)$, where each realization of any u_l belongs to a normed space $(U, \|\cdot\|_U)$. Denote $\bar{Y}_l = Y_l - Y_{l-1}$ for $l = 2, \dots, L$ and $\bar{Y}_1 = Y_1$. The MLMC-based PhIK prediction $\hat{y}(\mathbf{x})$ can be given as*

$$\hat{y}(\mathbf{x}) = \mu_{MLMC}(\mathbf{x}) + \sum_{i=1}^N \tilde{a}_i k_{MLMC}(\mathbf{x}, \mathbf{x}^{(i)}), \quad (22)$$

where

$$\mu_{MLMC}(\mathbf{x}) = \sum_{l=0}^L \frac{1}{M_l} \sum_{m=1}^{M_L} \bar{Y}_l(\mathbf{x});$$

$$k_{MLMC}(\mathbf{x}, \mathbf{x}')$$

$$= \sum_{l=0}^L \frac{1}{M_l - 1} \sum_{m=1}^{M_L} \left(\bar{Y}_l^m(\mathbf{x}) - \frac{1}{M_l} \sum_{m=1}^{M_L} \bar{Y}_l^m(\mathbf{x}) \right) \left(\bar{Y}_l^m(\mathbf{x}') - \frac{1}{M_l} \sum_{m=1}^{M_L} \bar{Y}_l^m(\mathbf{x}') \right);$$

and $\tilde{a}_i = ((\mathbf{C}_{MLMC} + \alpha \mathbf{I})^{-1}(\mathbf{y} - \boldsymbol{\mu}_{MLMC}))_i$, $\boldsymbol{\mu}_{MLMC} = (\mu_{MLMC}(\mathbf{x}^{(1)}), \dots, \mu_{MLMC}(\mathbf{x}^{(N)}))^T$, $(\mathbf{C}_{MLMC})_{ij} = k_{MLMC}(\mathbf{x}^{(i)}, \mathbf{x}^{(j)})$. Let \mathcal{L} , $g(\mathbf{x}; \omega)$, $\bar{g}(\mathbf{x})$, and $\|\cdot\|$ be given as in Theorem 2.1.

1) If $g(\mathbf{x}; \omega)$ is a deterministic function, i.e., $g(\mathbf{x}; \omega) = g(\mathbf{x})$, and u_l satisfies $\mathcal{L}u_l(\mathbf{x}; \omega) = g(\mathbf{x})$ for any $\omega \in \Omega$ and for $l = 1, \dots, L$, then $\mathcal{L}\hat{y}(\mathbf{x}) = g(\mathbf{x})$.

2) If Y_l satisfies $\|\mathcal{L}Y_l(\mathbf{x}; \omega) - g(\mathbf{x}; \omega)\| \leq \epsilon_l$ for $l = 1, \dots, L$, then

$$\|\mathcal{L}\hat{y}(\mathbf{x})\| \leq \sum_{l=1}^L C_l \epsilon_l + \sigma(g(\mathbf{x}; \omega^m)) \sum_{i=1}^N \tilde{a}_i \sigma(Y_L^m(\mathbf{x}^{(i)})), \quad (23)$$

where

$$C_l = \begin{cases} 1 + 2 \sum_{i=1}^N \tilde{a}_i \sqrt{\frac{M_l}{M_l - 1}} \sigma(\bar{Y}_l^m(\mathbf{x}^{(i)})), & l = L; \\ 2 + 2 \sum_{i=1}^N \tilde{a}_i \left(\sqrt{\frac{M_l}{M_l - 1}} \sigma(\bar{Y}_l^m(\mathbf{x}^{(i)})) + \sqrt{\frac{M_{l+1}}{M_{l+1} - 1}} \sigma(\bar{Y}_{l+1}^m(\mathbf{x}^{(i)})) \right), & 1 \leq l < L. \end{cases}$$

Of note, MLMC estimates for variance and higher-order single point (i.e., a fixed $\mathbf{x} \in \mathbb{R}^d$) statistical moments was proposed in [3, 5, 6]. The covariance estimate Eq. (18) proposed herein also can be used to estimate variance by setting $\mathbf{x}' = \mathbf{x}$. The systematic convergence analysis of the MLMC can be found in [22, 3, 8, 5, 6]. Other multifidelity methods, e.g., [21, 76], also can be used as long as they compute the mean and covariance efficiently.

2.4 Active learning

In this context, *active learning* (e.g., [9, 27, 59, 10]) is a process of identifying locations for additional observations that minimize the prediction error and reduce MSE or uncertainty. In the GPR framework, a natural way is to add observations at the locations corresponding to local maxima in $s^2(\mathbf{x})$, e.g., [19, 49]. Then, we can make a new prediction $\hat{y}(\mathbf{x})$ for $\mathbf{x} \in D$ and compute a new $\hat{s}^2(\mathbf{x})$ to select the next location for additional observation (see Algorithm 1). Such treatment differs from other sensor placement methods based on deterministic approximation of unknown fields (e.g., [74, 70]). This selection criterion is based on the statistical interpretation of the interpolation.

Notably, Algorithm 1 is a greedy algorithm to identify additional observation locations when some observations are affordable. It cannot guarantee to identify the optimal new observation locations. More sophisticated algorithms can be found in literature, e.g., [27, 30, 64], and PhIK is complementary to these methods because it provides the GP. Also, it is not necessary that the new observations are added one by one. Roughly speaking, if there are several maxima of $\hat{s}^2(\mathbf{x})$ and they are not clustered (to avoid potential ill-conditioning of \mathbf{C} in some cases), the observations at these locations can be added simultaneously. In this work, we add new observations one by one in the numerical examples for demonstration purposes. The efficiency of the active learning algorithm depends on the correlation $\text{Cor}\{Y(\mathbf{x}), Y(\mathbf{x}')\} = \text{Cov}\{Y(\mathbf{x}), Y(\mathbf{x}')\} / (\sigma(Y(\mathbf{x}))\sigma(Y(\mathbf{x}')))$. Intuitively, if the correlation is large, then adding a new observation will provide information in a large neighborhood of this location, reducing the MSE in a large region. An extreme example is that when $\text{Cor}\{Y(\mathbf{x}), Y(\mathbf{x}')\} \equiv 1$ (e.g., the correlation length of the GP is infinite), only one observation is needed

Algorithm 1 Active learning based on GPR

- 1: Specify the locations \mathbf{X} , corresponding observation \mathbf{y} , and the maximum number of observation N_{\max} affordable. The number of available observations is denoted as N .
 - 2: **while** $N_{\max} > N$ **do**
 - 3: Compute the MSE $\hat{s}^2(\mathbf{x})$ of MLE prediction $\hat{y}(\mathbf{x})$ for $\mathbf{x} \in D$.
 - 4: Locate the location \mathbf{x}_m for the maximum of $\hat{s}^2(\mathbf{x})$ for $\mathbf{x} \in D$.
 - 5: Obtain observation y_m at \mathbf{x}_m and set $\mathbf{X} = \{\mathbf{X}, \mathbf{x}_m\}$, $\mathbf{y} = (\mathbf{y}^\top, y_m)^\top$, $N = N + 1$.
 - 6: **end while**
 - 7: Construct the MLE prediction of $\hat{y}(\mathbf{x})$ on D using \mathbf{X} and \mathbf{y} .
-

to reconstruct the field. On the other hand, if the correlation is small (e.g., the correlation length of the GP is small), an observation can only influence a small neighborhood, then more observations are required to reduce the uncertainty in the prediction of the entire domain. An extreme example of this scenario is $\text{Cor}\{Y(\mathbf{x}), Y(\mathbf{x}')\} \equiv 0$. Unless we have observations everywhere, the MSE in the prediction at the locations with no observations is unchanged no matter how many observations we have because at these locations $\mathbf{c} = \mathbf{0}$ in Eq. (5).

There is an important difference between performance of Kriging and PhIK in the context of active learning. PhIK prediction on entire D can be written as $\hat{\mathbf{y}} = \boldsymbol{\mu}_{MC} + \sum_{i=1}^N \tilde{a}_i \mathbf{k}_{MC}^{(i)}$ (see Eq. (31)), where $\hat{\mathbf{y}} = \hat{y}(\mathbf{x})$, and $\boldsymbol{\mu}_{MC} = \mu_{MC}(\mathbf{x}) \mathbf{k}_{MC}^{(i)} = k(\mathbf{x}, \mathbf{x}^{(i)})$. Because $\boldsymbol{\mu}_{MC}$ and $\mathbf{k}_{MC}^{(i)}$ are linear combination of $\{\hat{Y}^m(\mathbf{x})\}_{m=1}^M$, PhIK prediction on the entire field D , i.e., $\hat{\mathbf{y}}$, is a linear combination of ensemble $\{\hat{Y}^m(\mathbf{x})\}_{m=1}^M$. Therefore, once this ensemble is given, the approximation space for the exact field is fixed, and adding more observation will not enlarge this space. It is expected that a stochastic model that can better describe the underlying system will result in more accurate PhIK prediction via providing a more appropriate approximation space $\text{span}\{\hat{Y}^m(\mathbf{x})\}_{m=1}^M$. In contrast, in Kriging method, adding a new observation $y^{(N+1)} = y(\mathbf{x}^{(N+1)})$ enlarges the approximation space from $\text{span}\{k(\mathbf{x}, \mathbf{x}^{(i)})\}_{i=1}^N$ to $\text{span}\{k(\mathbf{x}, \mathbf{x}^{(i)})\}_{i=1}^{N+1}$ (see Eq. (30)), which has the potential to increase the accuracy of the prediction if the kernel $k(\cdot, \cdot)$ is chosen appropriately. We refer interested readers to literatures on reproducing kernel Hilbert space for theoretical results on approximation, e.g., [73, 4].

In both methods, the error $\|\hat{\mathbf{y}} - \mathbf{y}\|$ converges to zeros asymptotically because both Kriging and PhIK predictions coincide with the exact field wherever noiseless observation is available. However, in general, there is no guarantee the error decreases monotonically for each newly added observation.

There is a large body of literature in statistics and machine learning on the *learning curve* that describes the average MSE over D as a function of N , the number of available observations, e.g., [72, 34, 62, 53]. Both noisy and noiseless scenarios have been studied, and we refer interested readers to the aforementioned literatures.

2.5 Some discussions

2.5.1 Potential drawbacks

The PhIK methods requires using multiple simulation results of a stochastic model, which can be costly when the model is complex. There are different types of methods, e.g., multifidelity methods, that help to reduce the cost of estimating statistics by incorporating information from costly high-fidelity simulations and cheaper low-fidelity simulations. The MLMC used in this work is one of such methods. We note that running simulations with different sets of random parameters is a typical step in studies like model calibration, uncertainty quantification, sensitivity analysis as pointed out in Section 2.2. Therefore, we can either use the simulation results in these studies directly, or adjust approaches in these areas that reduce the computational cost to PhIK. For example, a bifidelity method is used to dramatically reduce the cost of running simulations [71]. Again, the motivation of PhIK is to exploit existing physical models to maximally extracted information very limited measurement data.

Another drawback is that PhIK results in a GP conditioned on observation data and this GP depends on the stochastic model we use. If the model can not appropriately reflect the known information or model unknowns using random variables/fields, then PhIK may not work well. Further, when implementing the active learning using PhIK, the locations of new observations is mainly decided by the pattern of the standard deviation of simulation results. Therefore, it is possible that some important locations are not selected for acquiring new observation if this information is not reflected in the model.

2.5.2 Computational cost

After obtaining simulations results, PhIK compute the posterior mean and variance at a new location \mathbf{x}^* , i.e.,

$$\begin{aligned}\hat{y}(\mathbf{x}^*) &= \boldsymbol{\mu}(\mathbf{x}^*) + \mathbf{c}'_{N \times 1} \mathbf{C}_{N \times N}^{-1} (\mathbf{y} - \boldsymbol{\mu})_{N \times 1}, \\ \hat{s}^2(\mathbf{x}^*) &= \sigma^2(\mathbf{x}^*) - \mathbf{c}'_{N \times 1} \mathbf{C}_{N \times N}^{-1} \mathbf{c}_{N \times 1},\end{aligned}$$

where we omit the notation ‘‘MC’’ or ‘‘MLMC’’ and the subscripts describe the size of each vector or matrix. The cost of obtaining \mathbf{C} is $O(M \times N^2)$. We use the Cholesky decomposition for \mathbf{C} , the cost of which is $O(N^3)$. Vector \mathbf{c} is obtained by a matrix-vector multiplication, the cost of which is $O(M \times N)$. Therefore, to compute the $\hat{y}(\mathbf{x}^*)$ and $\hat{s}^2(\mathbf{x}^*)$ on all grid points is $O(DOF \times M + M \times N^2 + N^3 + DOF \times (M \times N + N^2)) = O(DOF \times M \times N + DOF \times N^2 + M \times N^2 + N^3)$. Since we consider complex system whose measurement is very expensive, so N is small (e.g., N is no more than 30 in our numerical examples) and $M \ll DOF$ (M is usually a few hundred). Therefore, the complexity is approximately $O(DOF)$. This is the same as Kriging in this scenario (small N). In our numerical examples to be shown in the next section, the largest DOF is 32,768 and it also has largest $M = 500$. Implementing PhIK method costs less than one second on a laptop with 2.9GHz Dual-Core Intel Core i5 using MATLAB without parallelization. For larger systems, one can use parallel computing package as well as hardware like GPU to accelerate the computing.

2.5.3 Connection with other methods

In general, a GPR model use the following regression model [54]:

$$Y(\mathbf{x}) = \sum_{j=1}^K \beta_j f_j(\mathbf{x}) + Z(\mathbf{x}), \quad (24)$$

where β_j 's are constant scalar, f_j 's are deterministic functions, and Z is a GP with zeros mean. Apparently, Y is a GP, and the observation data are considered to be collected from a realization of Y . But usually only a few data on this realization is collected. In ordinary Kriging, $K = 1$, $f_1(\mathbf{x}) \equiv 1$ and β as well as hyperparameters of Z are estimated from data in the BLUP setting, i.e., Y is identified from partial data of one of its realization. In PhIK, $K = 1$, $\beta = 1$, f_1 is the empirical mean function and Z 's covariance is the empirical covariance. In other words, we have several complete realizations of a random field (not necessarily Gaussian), and we use their empirical mean and covariance function to construct Y directly. In a nutshell, Kriging constructs GP using data (which is typically sparse) on a domain, while PhIK uses these data plus some realizations on the entire domain. In both scenarios, we can implement multifidelity methods to improve the computational efficiency.

The multifidelity may refer to low and high-resolution models based on the same equations (e.g., in the MLMC approach in the third numerical example) or models using different mathematical description [42], e.g., some low-fidelity model may neglect less important forces and average out fast processes. Multifidelity methods were shown to be efficient for computing one-point statistics (e.g., variance) for quantifying uncertainty [36, 20, 42]. In our work, we use MLMC to reduce the cost of estimating mean and two-point statistics (i.e., covariance).

Another type of multifidelity framework, e.g., [28, 44, 43, 41, 39], uses linear or nonlinear combination of *multiple* GPs to hierarchically construct a high-fidelity model. For example, the multifidelity GPR in [28, 44] assumes $Y(\mathbf{x}) = \rho(\mathbf{x})Y_{\text{low}}(\mathbf{x}) + Z(\mathbf{x})$ (we use two-fidelity case for illustration), where Y_{low} is a GP regressing

low-fidelity data and $\rho(x)$ is a deterministic scalar function. It can be interpreted as replacing $\sum_{j=1}^K \beta_j f_j(\mathbf{x})$ in Eq. (24) with a GP Y_{low} . This procedure can be repeated recursively as in [44, 43, 41]. This idea can be implemented in PhIK, too. For example, one can construct Y_{low} using low-fidelity simulations first, then use high-fidelity simulations as well as data to identify ρ and Z . Alternatively, one can construct Y_{low} using PhIK with multifidelity simulations as we show in this work, then identify Z using a predecided form of kernel function as in the aforementioned hierarchical method, an example of which is shown in [67].

The main difference between PhIK and the aforementioned methods in the context of multifidelity is that the latter considers multifidelity data $\mathbf{y} = (y^{(1)}, \dots, y^{(N)})$, while the former considers single fidelity data. In the purely data-driven setting, the aforementioned hierarchical methods, each data set is a small subset of a *single* realization of a random field at different fidelity level. These data are integrated to construct a random field on the entire domain. On the other hand, in PhIK, roughly speaking, we also have *multiple* realizations of different random fields on the entire domain, which are used to construct a random field on the entire domain associated with the data. In this construction procedure, data is not used. If we only have one realization from each stochastic model, then we have the same setting as the purely data-driven setting, and PhIK does not apply because we only have degenerate empirical statistics. Regarding the computational cost, Kriging is known to be expensive when the data set is large. The complexity in constructing a GP is $O(N^3)$, which can be further reduced, e.g., to $O(N)$, if special structure exists [47, 43, 41]. Of note, here $O(N)$ is the cost to identify the kernel function, and then the cost to compute the covariance matrix is $O(N^2)$. In the PhIK case, the cost of directly implementing the algorithm to construct the covariance matrix is $O(MN^2)$. As we usually set M to be a few hundred, when N is large, the complexity is $O(N^2)$. The cost of computing the empirical mean vector at observation locations is MN multiplied by a constant, so the complexity is $O(N)$. Therefore, the complexity of “training” PhIK is $O(N^2)$, which is the same as the purely data-driven methods.

We also note that merging model and data can be categorized as a multi-resolution and multifidelity modeling task, where a real system is represented as a set of models of different resolutions at different abstraction levels from the viewpoint of simulation objectives [13, 24, 48]. In our cases, the data is considered as a high-fidelity “model” and the stochastic model is treated as a low-fidelity model.

Finally, the well-known work [32] built connection between a specific family of fractional SPDE and the Matern random field in that the solution of the SPDE is a Gaussian random field with a Matern kernel. Hence, one can solve the SPDE to multiple times and use the empirical mean and covariance to construct the corresponding GP. Our method can be considered as an extension of this approach as it uses any stochastic model’s empirical mean and covariance to construct a GP.

3 Numerical examples

We present two numerical examples to demonstrate the performance of PhIK. Both numerical examples are two-dimensional in physical space. In the first two examples, we use the MC-based PhIK introduced in Section 2.2, and in the third one, we employ the MLMC-based PhIK presented in Section 2.3. We compare PhIK with the ordinary Kriging (in the following, we refer to it as Kriging). In the Kriging method, we tested the Gaussian kernel and Matérn kernel. We do not observe significant difference in the results and only report solutions obtained with the Gaussian kernel. All Kriging results are obtained by the MATLAB package GPML [52]. In each example, we use $y(\mathbf{x})$ to denote the reference solution, $\hat{y}(\mathbf{x})$ to denote the posterior mean, which is typically used as the prediction or reconstruction result, and $\hat{s}(\mathbf{x})$ to denote the posterior standard deviation, which can be interpreted as the uncertainty in the prediction. The simulations of stochastic model are denoted as $\{Y^m(\mathbf{x})\}_{m=1}^M$ for the MC-based PhIK. Similarly, in the MLMC-based PhIK, $\{Y_L^m(\mathbf{x})\}_{m=1}^{M_L}$ and $\{Y_H^m(\mathbf{x})\}_{m=1}^{M_H}$ denote simulations of low- and high-resolution simulations, respectively.

3.1 Branin function

We consider the following modified Branin function [19]:

$$f(x, y) = a(\bar{y} - b\bar{x}^2 + c\bar{x} - r)^2 + g(1 - p) \cos(\bar{x}) + g + qx, \quad (25)$$

where

$$\bar{x} = 15x - 5, \bar{y} = 15y, (x, y) \in D = [0, 1] \times [0, 1],$$

and

$$a = 1, b = 5.1/(4\pi^2), c = 5/\pi, r = 6, g = 10, p = 1/(8\pi), q = 5.$$

The contour of f and eight randomly chosen observation locations are presented in Figure 1(a). The function f is evaluated on a 41×41 uniform grid, and we denote the resulting discrete field (a 41×41 matrix) as $y(\mathbf{x})$. We will compare $\hat{y}(\mathbf{x})$, $\hat{s}(\mathbf{x})$ and $\hat{y}(\mathbf{x}) - y(\mathbf{x})$ by different methods.

3.1.1 Field reconstruction

We first use Kriging with the eight observation data sets. Figure 1 (b) presents the resulting $\hat{y}(\mathbf{x})$, and Figure 1 (c) depicts corresponding $\hat{s}(\mathbf{x})$. The difference $\hat{y}(\mathbf{x}) - y(\mathbf{x})$ is shown in Figure 1 (d), which quantifies the $\hat{y}(\mathbf{x})$ deviation from the ground truth. Apparently, this reconstruction deviates considerably from $y(\mathbf{x})$ in Figure 1 (a), especially in the region $[0, 0.5] \times [0.5, 1]$. This is consistent with Figure 1(c) as $\hat{s}(\mathbf{x})$ is large in this region. This is because there is no observation in this region.

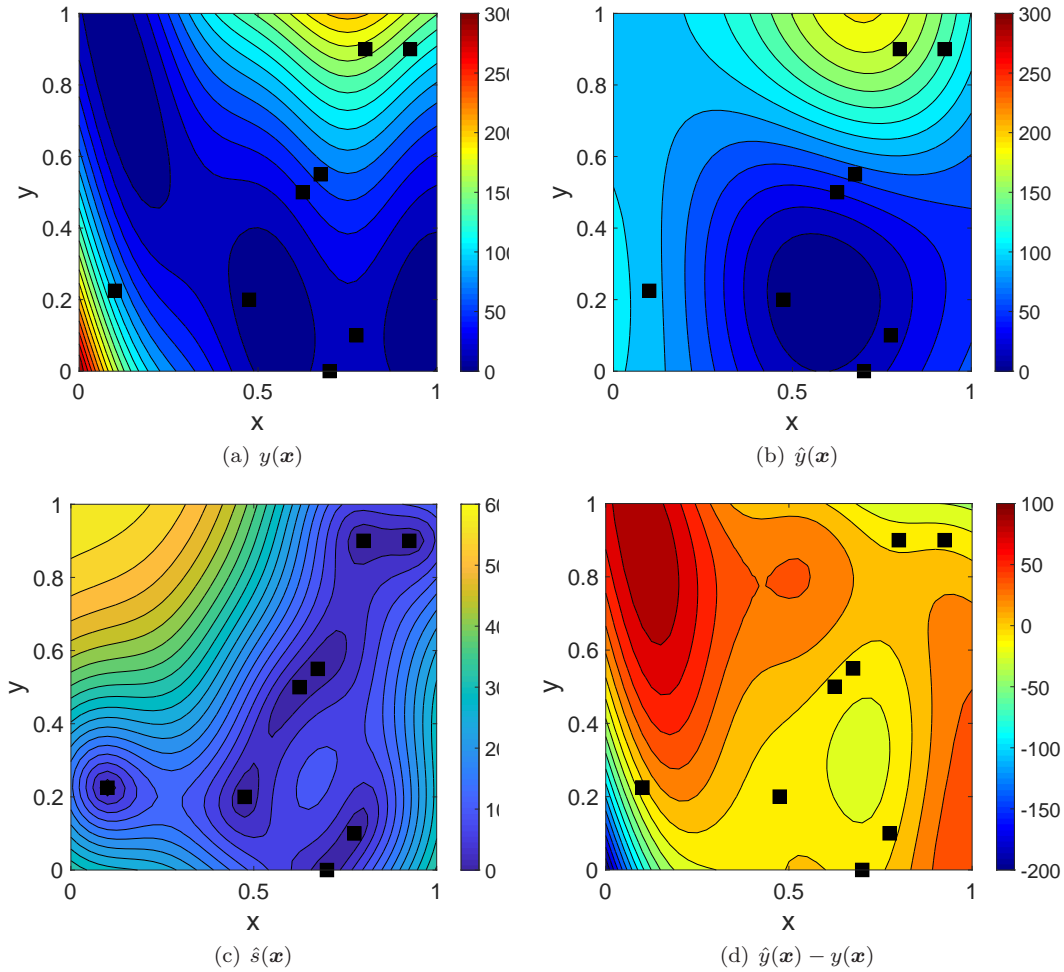


Figure 1: Branin function: reconstruction of the modified Branin function by Kriging: (a) exact field $y(\mathbf{x})$; (b) $\hat{y}(\mathbf{x})$; (c) $\hat{s}(\mathbf{x})$; (d) difference $\hat{y}(\mathbf{x}) - y(\mathbf{x})$.

Next, we assume that based on “domain knowledge”, $f(x, y)$ is partially known, e.g., its form is known, but the coefficients b and q are unknown. Then, we treat these coefficients as random fields \hat{b} and \hat{q} , which indicates that the field f is described by a random function $\hat{f} : D \times \Omega \rightarrow \mathbb{R}$:

$$\hat{f}(x, y; \omega) = a(\bar{y} - \hat{b}(x, y; \omega)\bar{x}^2 + c\bar{x} - r)^2 + g(1 - p) \cos(\bar{x}) + \hat{g} + \hat{q}(x, y; \omega)x, \quad (26)$$

$$\hat{b}(x, y; \omega) = b \left\{ 0.9 + \frac{0.2}{\pi} \sum_{i=1}^3 \left[\frac{1}{4i-1} \sin((2i-0.5)\pi x) \xi_{2i-1}(\omega) + \frac{1}{4i+1} \sin((2i+0.5)\pi y) \xi_{2i}(\omega) \right] \right\},$$

$$\hat{q}(x, y; \omega) = q \left\{ 1.0 + \frac{0.6}{\pi} \sum_{i=1}^3 \left[\frac{1}{4i-3} \cos((2i-1.5)\pi x) \xi_{2i+5}(\omega) + \frac{1}{4i-1} \cos((2i-0.5)\pi y) \xi_{2i+6}(\omega) \right] \right\},$$

and $\{\xi_i(\omega)\}_{i=1}^{12}$ are i.i.d. Gaussian random variables with zero mean and unit variance. Further, we allow for the model error by setting $\hat{g} = 20$, which is different from $g = 10$ in Eq. (26). We use this partial knowledge to compute the mean and covariance function of \hat{f} by generating $M = 100$ samples of $\xi_i(\omega)$ and evaluating \hat{f} on the 41×41 uniform grid for each sample of $\xi_i(\omega)$. Figure 2 (a)-(c) present $\hat{y}(\mathbf{x})$, $\hat{s}(\mathbf{x})$, and $\hat{y}(\mathbf{x}) - y(\mathbf{x})$. These results are much better than those obtained by Kriging as both $\hat{s}(\mathbf{x})$ and $|\hat{y}(\mathbf{x}) - y(\mathbf{x})|$ are much smaller. More significantly, the $\hat{s}(\mathbf{x})$ in PhIK is much smaller than Kiriging in the $[0, 0.5] \times [0.5, 1]$ subdomain with no observations. This is because in PhIK, the covariance matrix is computed based on standard deviation of the physics-based model. Figure 2 (d) shows the standard deviation of $\{Y^m(\mathbf{x})\}_{m=1}^M$ denoted as $\sigma_{MC}(\mathbf{x})$. Note that σ_{MC} is a measure of uncertainty in the physical model \hat{f} . This plot demonstrates that $\hat{s}(\mathbf{x})$ (which is a measure of uncertainty in PhIK) has a similar pattern as $\sigma_{MC}(\mathbf{x})$, but with smaller magnitude. It indicates that PhIK reduces uncertainty by conditioning the prediction model \hat{f} on observations.

3.1.2 Active learning

After obtaining $\hat{s}(\mathbf{x})$, we use Algorithm 1 to perform active learning by adding one by one new observations of f at (x, y) where $\hat{s}(\mathbf{x})$ has maximum. Figure 3 displays locations of additional observations (marked as stars) and results by Kriging and PhIK when eight new observations are added. In this figure, the first row compares $\hat{y}(\mathbf{x})$ by these two methods, the second row compares $\hat{s}(\mathbf{x})$, and the last row compares $\hat{y}(\mathbf{x}) - y(\mathbf{x})$. As expected, the reconstruction accuracy increases as more observations are added. The PhIK still outperforms Kriging, but the difference is less significant compared with results in Figures 1 and 2. Notably, the active learning with Kriging places new observation points on all four boundaries. This illustrates that the GPR is more accurate for interpolation than extrapolation. Because most original observations are within the domain, the results are extrapolated toward the boundary. In contrast, the active learning algorithm with PhIK places most new observation points near the right boundary, where the $\sigma_{MC}(\mathbf{x})$ is large. This further confirms the influence of the physical model on the PhIK algorithm.

Figure 4 shows the relative error $\|\hat{y}(\mathbf{x}) - y(\mathbf{x})\|_2 / \|y(\mathbf{x})\|_2$ in Kriging and PhIK as a function of the observation numbers, where the first eight are the “original” observations and the rest are added according to the active learning algorithm. With the original eight observations, the PhIK result (about 8% error) is much better than the Kriging (more than 50% error). As more observations are added by the active learning algorithm, the error of Kriging decreases quickly to nearly 1% (24 observations). The error of PhIK reduces from 8% to 4% (10 observations), then it slowly reduces to 3% (24 observations). According to the discussion in Section 2.4, this is because Kriging introduces a new basis function $k(\mathbf{x}, \mathbf{x}^{(N+1)})$ when a new observation at location $\mathbf{x}^{(N+1)}$ is available and the Gaussian kernel is suitable for approximating smooth functions like

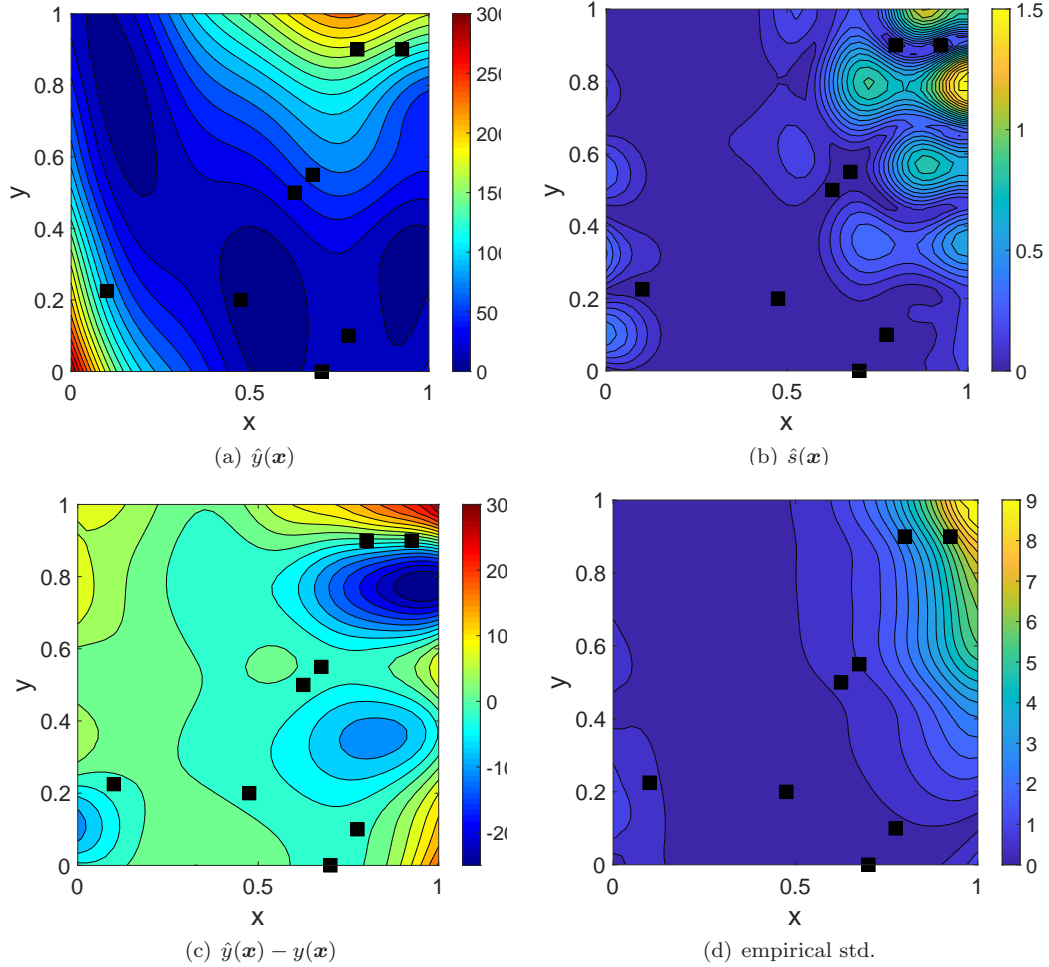


Figure 2: Branin function: reconstruction of the field by PhIK: (a) $\hat{y}(\mathbf{x})$; (b) $\hat{s}(\mathbf{x})$; (c) $\hat{y}(\mathbf{x}) - y(\mathbf{x})$; (d) standard deviation of $\{Y^m(\mathbf{x})\}_{m=1}^M$.

f. On the other hand, using 12 observations is sufficient to identify an accurate approximation of the exact field in the space spanned by $\{Y^m(\mathbf{x})\}_{m=1}^M$, and adding few observations doesn't result in significant change. This is why the convergence is very slow with more than 12 observations. We also note that if we use empirical mean only to approximate $y(\mathbf{x})$, the relative error is 18%. This indicates that observation data are incorporated effectively to improve the prediction accuracy.

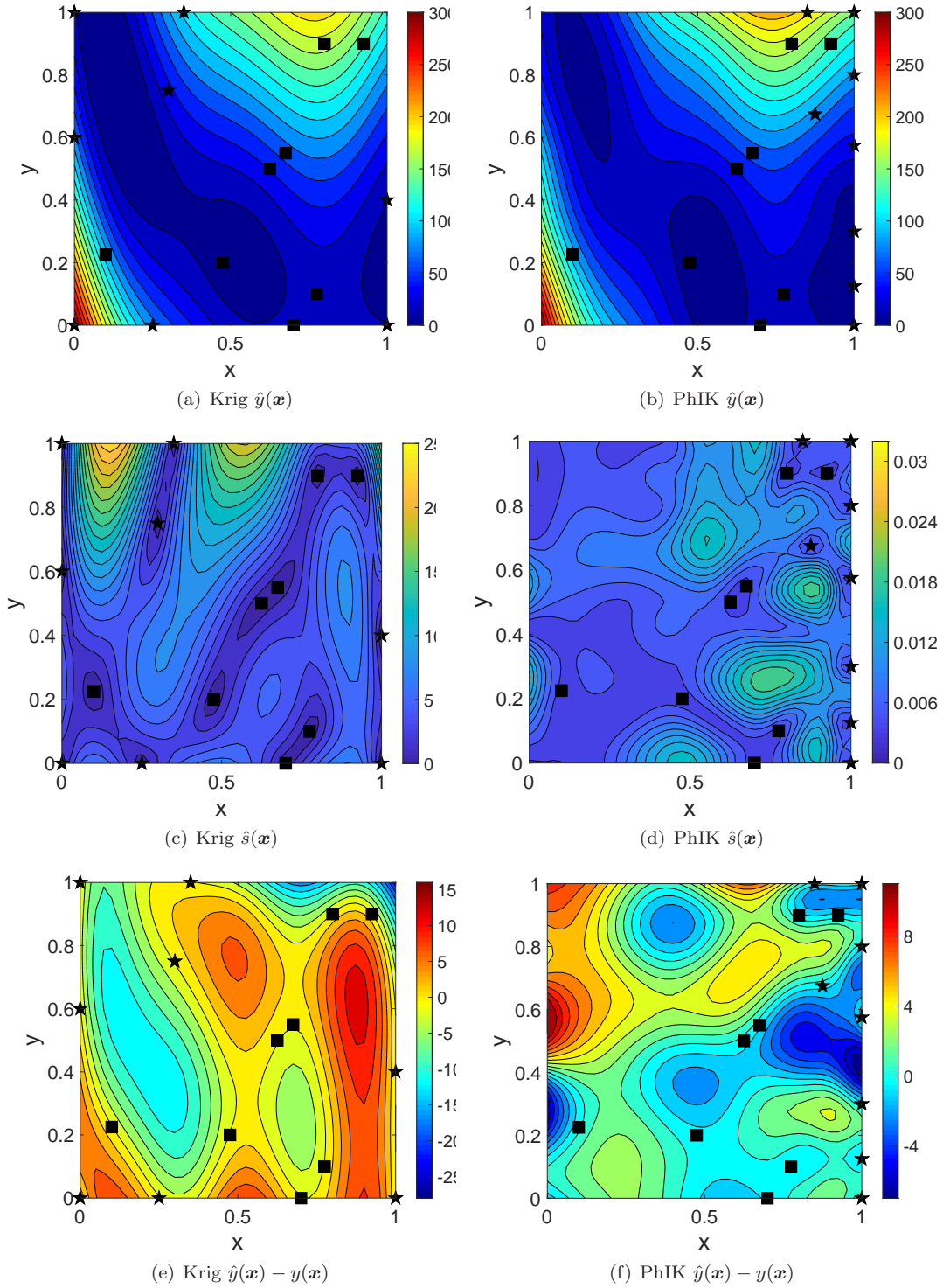


Figure 3: Branin function: reconstruction of the field by PhIK via active learning. Black squares mark the locations of the original eight observations, and stars are newly added observations. First row: $\hat{y}(\mathbf{x})$; second row: $\hat{s}(\mathbf{x})$; third row: $\hat{y}(\mathbf{x}) - y(\mathbf{x})$.

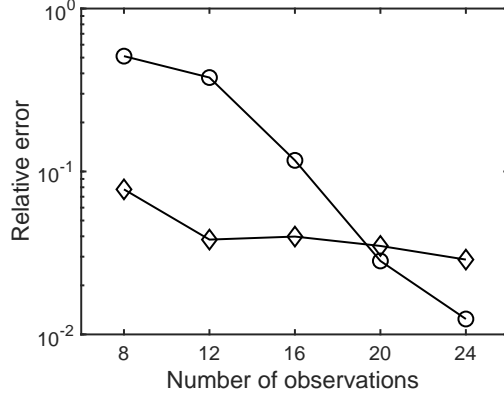


Figure 4: Branin function: relative error of the reconstructed field $\|\hat{y}(\mathbf{x}) - y(\mathbf{x})\|_2 / \|y(\mathbf{x})\|_2$ using Kriging (“o”) and PhIK (“◊”) with different numbers of total observations via active learning.

3.2 Heat transfer in a hallow sphere

In the second example, we consider a heat transfer problem in a hallow sphere $D = B_4(0) - B_2(0)$, where $B_r(0)$ is a ball with radius r centered at 0. The governing equation is

$$\begin{cases} \frac{\partial u(\mathbf{x}, t)}{\partial t} - \nabla \cdot (\kappa \nabla u(\mathbf{x}, t)) = 0, & \mathbf{x} \in D, \\ \kappa \frac{\partial u(\mathbf{x}, t)}{\partial \mathbf{n}} = \theta^2 (\pi - \theta)^2 \phi^2 (\pi - \phi)^2, & \text{if } \|\mathbf{x}\|_2 = 4 \text{ and } \phi \geq 0, \\ \kappa \frac{\partial u(\mathbf{x}, t)}{\partial \mathbf{n}} = 0, & \text{if } \|\mathbf{x}\|_2 = 4 \text{ and } \phi < 0, \\ u(\mathbf{x}, t) = 0, & \text{if } \|\mathbf{x}\|_2 = 2, \end{cases} \quad (27)$$

where \mathbf{n} is the outward-pointing normal, θ and ϕ are azimuthal and elevation angles of points in the sphere. The initial condition is 0 for all points. The exact heat conductivity is $\kappa = 1.0 + \exp(0.05u)$. We solve this equation using MATLAB’s PDE Tool Box [1]. Specifically, we use quadratic element with DOF being 12,854, and set $y(\mathbf{x}) = u(\mathbf{x}, 10)$, which is shown in Figure 5.

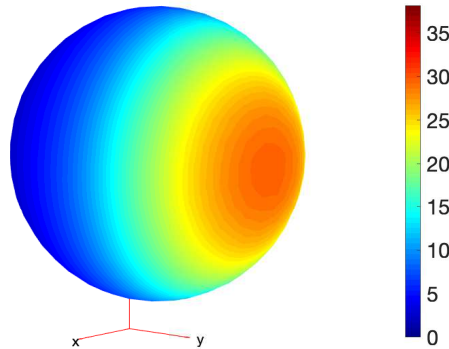


Figure 5: Heat transfer: ground truth $y(\mathbf{x})$.

3.2.1 Field reconstruction

We assume that accurate observation data are available at six locations: $\mathbf{X} = \{(3, 0, 0), (-3, 0, 0), (0, 3, 0), (0, -3, 0), (0, 0, 3), (0, 0, -3)\}$, which enables us to use Kriging to reconstruct $y(\mathbf{x})$. Figure 6 (a) present the $\hat{y}(\mathbf{x})$ of Kriging, which significantly deviates from $y(\mathbf{x})$. Figure 7 (a) shows the $\hat{s}(\mathbf{x})$ of Kriging, which is close to 2 at many points. Next, we assume that the exact $\kappa(u)$ is not known, and a stochastic model is proposed as $\kappa(u; \omega) = 2.0 + u\xi(\omega)$, where $\xi \sim \mathcal{U}[0.2, 0.4]$. We generate $M = 100$ samples of ξ and solve the heat equation 100 times to obtain corresponding simulation results $\{Y^m(\mathbf{x})\}_{m=1}^M$. Figure 6 (b) shows that the empirical mean of $\{Y^m(\mathbf{x})\}_{m=1}^M$ deviate significantly from $y(\mathbf{x})$, the relative error is 17%. Figure 7 (b) illustrates the standard deviation $\sigma_{MC}(\mathbf{x})$ of $\{Y^m(\mathbf{x})\}_{m=1}^M$ at each point. It demonstrates that $\sigma_{MC}(\mathbf{x})$ is large in the region with higher temperature, which is consistent with the setup of $\kappa(u; \xi(\omega))$. Then, the PhIK results are shown in Figure 6 (c) and Figure 7 (c). PhIK's $\hat{y}(\mathbf{x})$ matches the reference solution $y(\mathbf{x})$ quite well and its $\hat{s}(\mathbf{x})$ is rather small.

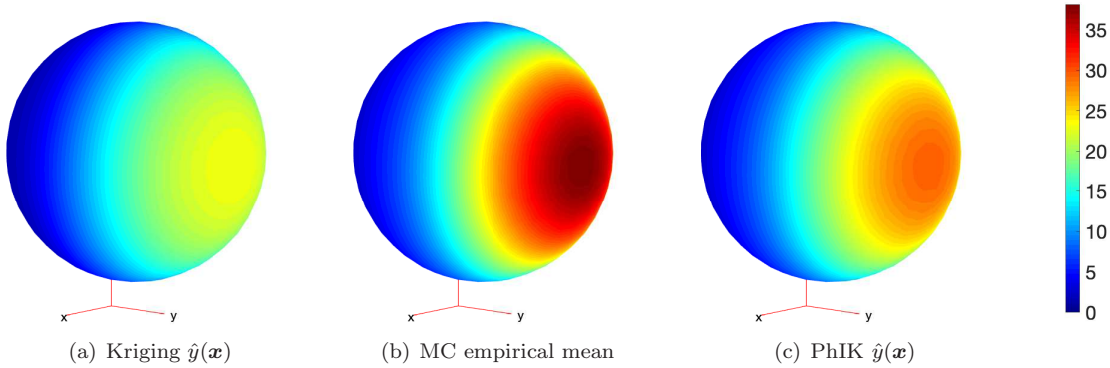


Figure 6: Heat transfer: mean values of different methods.

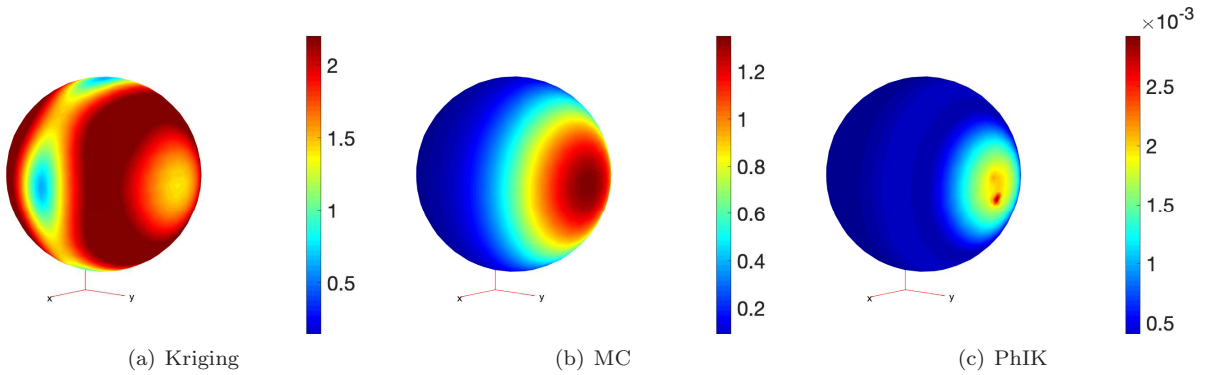


Figure 7: Heat transfer: standard deviations of different methods.

3.2.2 Active learning

Moreover, we use the active learning algorithm to add new observation data one by one. The location of the six original locations are shown in Figure 8 (a). The first six new locations identified by active learning with Kriging is shown in Figure 8 (b) marked as stars. These stars are actually near the boundary of domain D . On the other hand, the new locations identified by active learning with PhIK, illustrated in Figure 8 (c) are located in the region with large σ_{MC} as shown in Figure 7 (b).

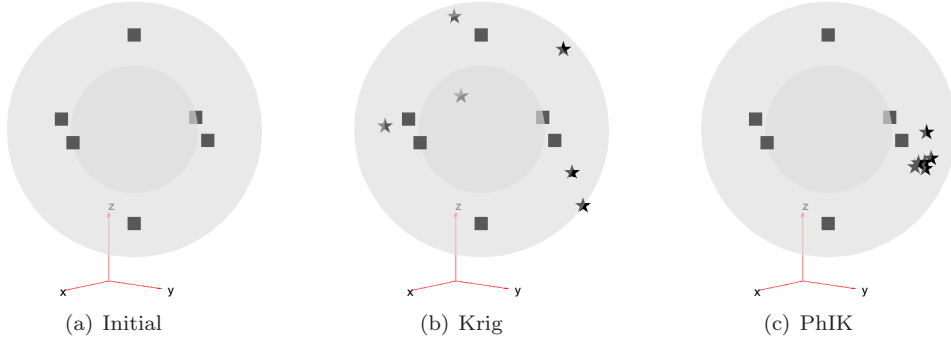


Figure 8: Heat transfer: additional observation locations identified via active learning.

Finally, we keep adding new observations and present the change of relative error in Figure 9. For this example, PhIK dramatically outperforms Kriging, as the accuracy of the former is three orders of magnitude better than the latter. Also, in both methods, the relative errors reduces as more observation data are available. Moreover, as an example of preserving linear constraint, the Dirichlet boundary condition is

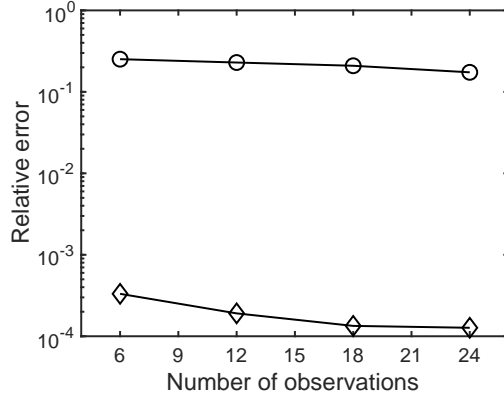


Figure 9: Heat transfer: relative error of reconstructed field $\|\hat{y}(\mathbf{x}) - y(\mathbf{x})\|_2 / \|y(\mathbf{x})\|_2$ using Kriging (“o”) and PhIK (“◊”) with different numbers of total observations via active learning.

preserved quite well in $\hat{y}(\mathbf{x})$ as the maximum of $\hat{y}(\mathbf{x})$ at grids located on the inner sphere is less than 0.01.

3.3 Solute transport in heterogeneous porous media

In the third example, we consider steady-state flow, and advection and dispersion of conservative tracer with concentration $C_e(\mathbf{x}, t)$ in a heterogeneous porous medium with known initial and boundary conditions and the unknown hydraulic conductivity $K(\mathbf{x})$. We assume that measurements of $C_e(\mathbf{x}, t)$ are available at several locations at different times. The flow and transport in porous media can be described by conservation laws, including a combination of the continuity equation and Darcy law:

$$\begin{cases} \nabla \cdot [K(\mathbf{x}; \omega) \nabla h(\mathbf{x}; \omega)] = 0, & \mathbf{x} \in D, \\ \frac{\partial h(\mathbf{x}; \omega)}{\partial \mathbf{n}} = 0, & x_2 = 0 \text{ or } x_2 = L_2, \\ h(x_1 = 0, x_2; \omega) = H_1 \text{ and } h(x_1 = L_1, x_2; \omega) = H_2, \end{cases} \quad (28)$$

where $D = [0, L_1] \times [0, L_2] = [0, 256] \times [0, 128]$, the unknown conductivity is modeled as the random log-normally distributed field $K(\mathbf{x}; \omega) = \exp(Z(\mathbf{x}; \omega))$ with the known exponential covariance function

$\text{Cov}\{Z(\mathbf{x}), Z(\mathbf{x}')\} = \sigma_Z^2 \exp(-|\mathbf{x} - \mathbf{x}'|/l_z)$ with the variance $\sigma_Z^2 = 2$, correlation length $l_z = 5$, $h(\mathbf{x}; \omega)$ is the hydraulic head, and $\omega \in \Omega$. The solute transport is governed by the advection-dispersion equation [17, 31]:

$$\begin{cases} \frac{\partial C(\mathbf{x}, t; \omega)}{\partial t} + \nabla \cdot (\mathbf{v}(\mathbf{x}; \omega)C(\mathbf{x}, t; \omega)) = \\ \quad \nabla \cdot \left[\left(\frac{D_w}{\tau} + \boldsymbol{\alpha} \|\mathbf{v}(\mathbf{x}; \omega)\|_2 \right) \nabla C(\mathbf{x}, t; \omega) \right], & \mathbf{x} \text{ in } D, \\ C(\mathbf{x}, t = 0; \omega) = \delta(\mathbf{x} - \mathbf{x}^*), \\ \frac{\partial C(\mathbf{x}; \omega)}{\partial \mathbf{n}} = 0, & x_2 = 0 \text{ or } x_2 = L_2 \text{ or } x_1 = L_1, \\ C(x_1 = 0, x_2; \omega) = 0, \end{cases} \quad (29)$$

where $C(\mathbf{x}, t; \omega)$ is the solute concentration defined on $D \times [0, T] \times \Omega$, the solute is instantaneously injected at $\mathbf{x}^* = (50, 64)$, $\mathbf{v}(\mathbf{x}; \omega) = -K(\mathbf{x}; \omega)\nabla h(\mathbf{x}; \omega)/\phi$ is the average pore velocity, ϕ is the porosity, D_w is the diffusion coefficient, τ is the tortuosity, and $\boldsymbol{\alpha}$ is the dispersivity tensor with the diagonal components α_L and α_T . In the present work, the transport parameters are set to $\phi = 0.317$, $\tau = \phi^{1/3}$, $D_w = 2.5 \times 10^{-5}$ m²/s, $\alpha_L = 5$ m, and $\alpha_T = 0.5$ m.

We generate $M = 1000$ realizations of $Z(\mathbf{x})$ using the SGSIM (sequential Gaussian simulation) code [14] and solve the governing equations for each realization of $K(\mathbf{x}) = \exp(Z(\mathbf{x}))$ using the finite volume code STOMP (subsurface transport over multiple phases) [60] with the mesh size $1\text{m} \times 1\text{m}$, i.e., 256×128 uniform grids. Here, we study the results at $t = 8$ days. The reference solution is generated as one of the 1000 solutions of the governing equations and is shown in Figure 10 with observation locations. We assume that six uniformly spaced observations are available near the domain boundary, and nine randomly placed observations are given (also illustrated in the domain of interest in pr

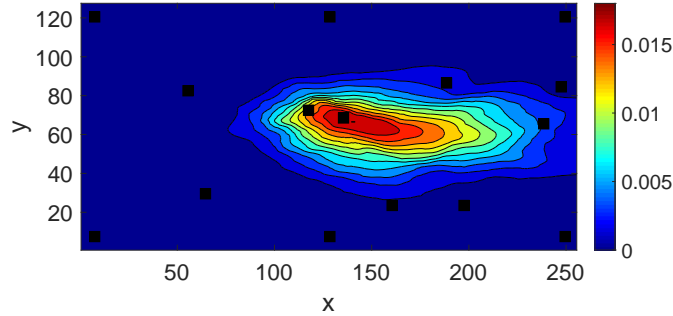


Figure 10: Solute transport: reference solution of the solute concentration when $t = 8$ days and observation locations (black squares).

3.3.1 Field reconstruction

We first use Kriging to reconstruct $y(\mathbf{x})$ using 15 observations. Figures 11 (a) and (b) present $\hat{y}(\mathbf{x})$ and the error $\hat{y}(\mathbf{x}) - y(\mathbf{x})$. We can see that Kriging performs poorly, and the relative error is larger than 40%. Next, we assume that only 10 simulations (i.e., $M_H = 10$) on 256×128 uniform grids are available and use them in the MC-based PhIK to reconstruct $y(\mathbf{x})$. Specifically, the mean and covariance matrix are computed from Eqs. (9) and (10) using ensembles $\{Y_H^m(\mathbf{x})\}_{m=1}^{M_H}$. Figure 11(c) and (d) present corresponding $\hat{y}(\mathbf{x})$ and $\hat{y}(\mathbf{x}) - y(\mathbf{x})$, respectively. These results are better than the Kriging as the relative error is around 26%. Finally, we include $M_L = 500$ coarse-resolution simulations with 64×32 uniform grids to use MLMC Eqs. (15) and (18), to approximate the mean and covariance. The corresponding $\hat{y}(\mathbf{x})$ and $\hat{y}(\mathbf{x}) - y(\mathbf{x})$ are presented in Figure 11(e) and (f), respectively. Adding the coarse simulations significantly improves

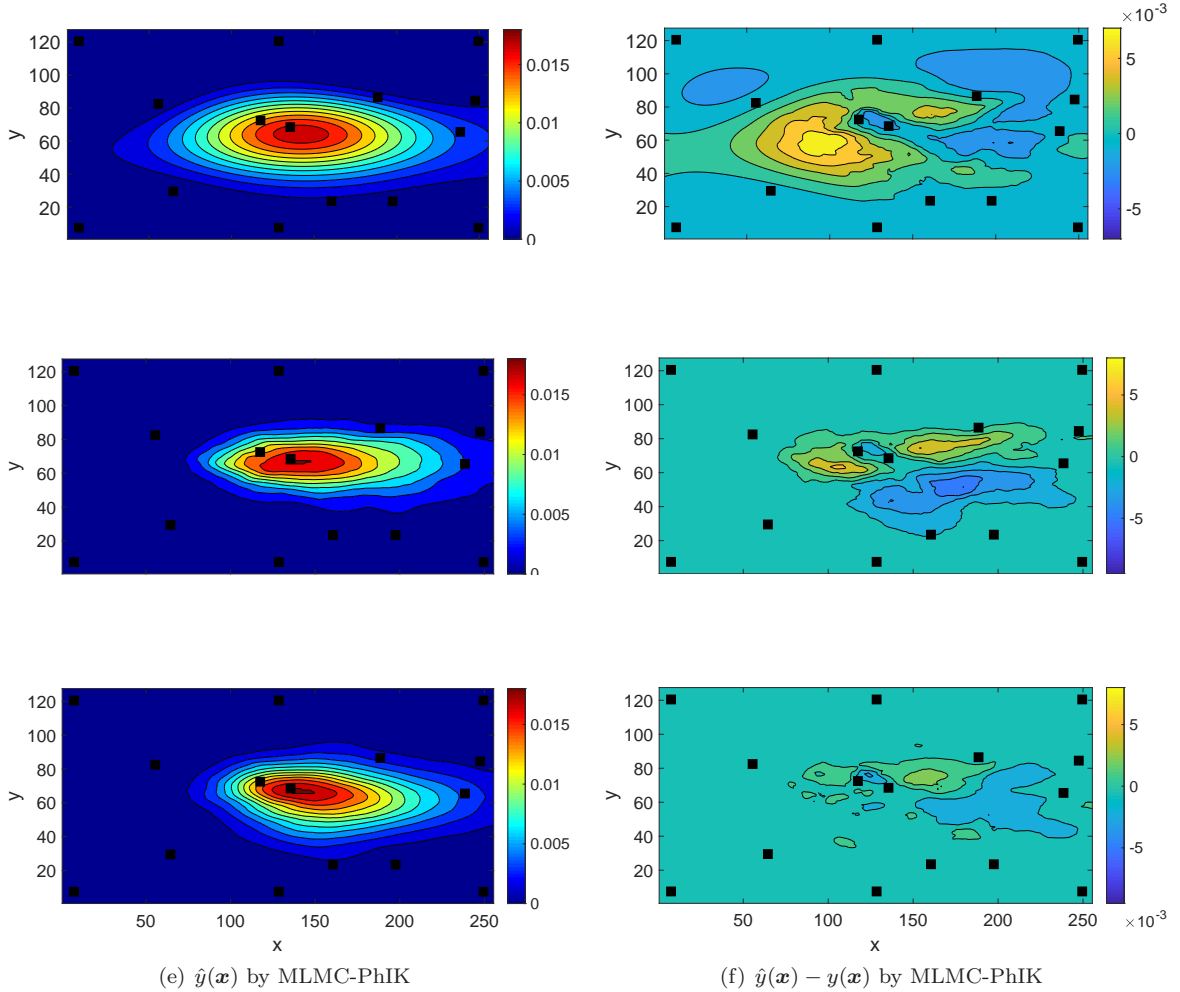


Figure 11: Solute transport: reconstructed solute concentration field $\hat{y}(\mathbf{x})$ by Kriging, MC-based PhIK with 10 high-resolution simulations, MLMC-based PhIK with 10 high-resolution (mesh size $1\text{m} \times 1\text{m}$) simulations and 500 low-resolution (grid size $4\text{m} \times 4\text{m}$) simulations, and their difference from the exact field $\hat{y}(\mathbf{x}) - y(\mathbf{x})$. Black squares are the observation locations.

Next, we study how the MLMC-based PhIK's accuracy depends on the number of high-resolution simulations M_H for the fixed number of low-resolution simulations $M_L = 500$. Figure 12(a) shows how the MLMC-based PhIK error $\|\hat{y}(\mathbf{x}) - y(\mathbf{x})\|_2 / \|y(\mathbf{x})\|_2$ decreases with increasing M_H . For comparison, we also compute error in the MC-based PhIK for the same number of M_H . It is clear that MC-based PhIK is less accurate than MLMC-based PhIK, especially for small M_H . Also, the smaller error in MLMC-based PhIK is achieved with a smaller computational cost than that of MC-based PhIK. In this example, the number of degrees of freedom in the low-resolution simulation is 1/16 of that in the high-resolution simulation. As we use an implicit scheme for the dispersion operator and an explicit scheme for the advection operator, according to the CFL condition, the time step in a low-resolution simulation is approximately four times larger than the time step in a high-resolution simulation. Therefore, the computational cost of a high-resolution simulation is at least 64 times that of a low-resolution simulation and the cost of 500 low-resolution simulations is less than eight high-resolution ones. Thus, for the considered problem, the MLMC-based PhIK using 10 high-

resolution and 500 low-resolution simulations is less costly than MC-based PhIK with 18 high-resolution simulations, while its accuracy is better than the latter with 90 high-resolution simulations (as shown in Figure 12(a)). Here, the accuracy of MLMC-based PhIK changes slowly as M_H increase from 20 to 90. This can be partially explained by examining the mean and covariance computed from MLMC. We use the mean and covariance of 5000 high-resolution simulations as reference and compare them with results by MLMC, respectively, in Figure 12(b). The differences are normalized by the $\|y(\mathbf{x})\|_2$ to investigate their influence on the MLMC-based PhIK’s accuracy. Here, we abuse the notation to set $\|\mathbf{c}(\mathbf{x})\|_F = (\sum_{\mathbf{x} \in D} \|\mathbf{c}(\mathbf{x})\|_2^2)^{1/2}$, where $\mathbf{c}(\mathbf{x})$ is the vector used in GPR prediction. It is clear that the influence from the difference in estimating the $\mathbf{c}(\mathbf{x})$ (triangles) is very small, and difference between the covariance matrix (not shown) is even smaller than the difference in $\mathbf{c}(\mathbf{x})$ because the k th row of \mathbf{C} is $\mathbf{c}(\mathbf{x}^{(k)})$. The difference in estimating the mean (squares) changes slowly when the number of high-resolution simulations is larger than 30 which is consistent with the trend of the diamonds in Figure 12(a).

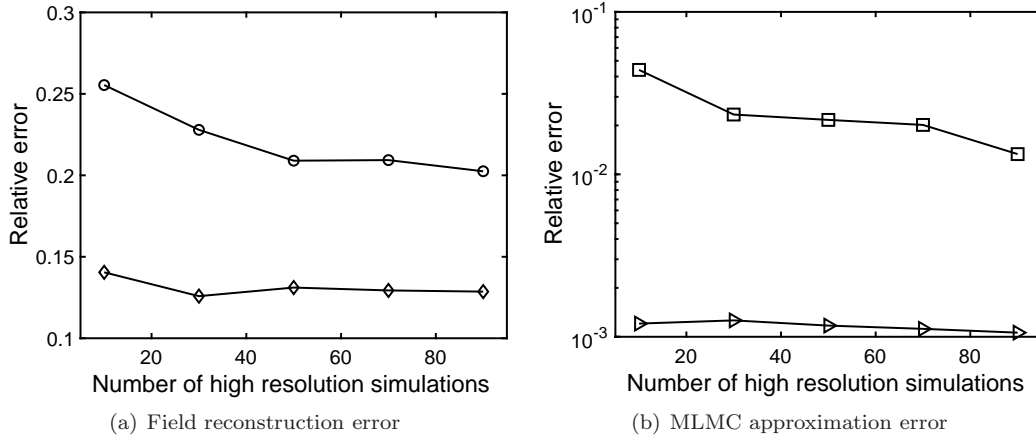


Figure 12: Solute transport: (a) Relative error of solute concentration $\|\hat{y}(\mathbf{x}) - y(\mathbf{x})\|_2 / \|y(\mathbf{x})\|_2$ by PhIK using different numbers of high-resolution simulations (mesh size $1\text{m} \times 1\text{m}$) only (“o”) and 500 low-resolution simulations (mesh size $4\text{m} \times 4\text{m}$) in addition to different numbers of high-resolution simulations (“d”). (b) $\|\mu_{MC}(\mathbf{x}) - \mu_{MLMC}(\mathbf{x})\|_2 / \|y(\mathbf{x})\|_2$ (“□”) and $\|\mathbf{c}_{MC}(\mathbf{x}) - \mathbf{c}_{MLMC}(\mathbf{x})\|_F / \|y(\mathbf{x})\|_2$ (“▷”).

Moreover, we denote the cost of each single low-fidelity simulation as C_L and the cost of each high-fidelity simulation as C_H . The total cost of simulations for MC-based PhIK is $C_H M$, where $M \approx M_L$, while the total cost of simulations for MLMC-based PhIK is $C_H M_H + C_L M_L$. The cost ratio (MLMC cost over MC cost) is approximately $M_H / M_L + C_L / C_H$. In this specific case, $M_H / M_L = 10 / 500 = 0.02$, and $C_L / C_H = 1 / 64 = 0.015625$. So the ratio of the cost is 0.035, i.e., 18 high-resolution simulations against 500 ones.

3.3.2 Active learning

We now compare the performance of the active learning algorithm based on Kriging and MLMC-based PhIK with ensembles $\{Y_H^m(\mathbf{x})\}_{m=1}^{M_H}$ and $\{Y_L^m(\mathbf{x})\}_{m=1}^{M_L}$ with $M_H = 10$, $M_L = 500$. Because we demonstrated that MLMC-based PhIK is more accurate and less costly than MC-based PhIK, we do not use the latter in this comparison. Figures 13 shows $\hat{s}(\mathbf{x})$ for Kriging, and MLMC-PhIK, both using the initial 15 observations (locations are denoted by squares). Note that $\hat{s}(\mathbf{x})$ in MLMC-PhIK is much smaller than that in Kriging and the locations of local maxima differ.

Next, we use Algorithm 1 in combination with Kriging MLMC-based PhIK to add new observations one by one. In these figures, the initial 15 observation locations are marked as squares and new locations are marked as stars. Figure 14 compares these results when 15 new observations are added. It shows that MLMC-based PhIK consistently outperforms Kriging as quantitatively confirmed by the comparison

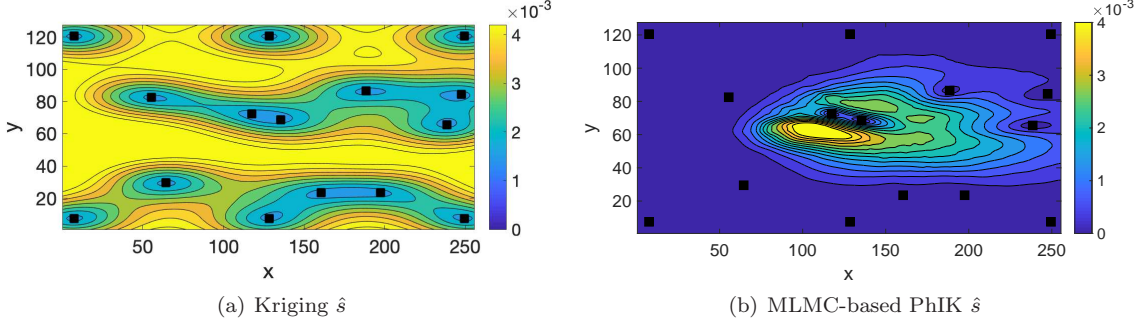


Figure 13: Solute concentration: (a) $\hat{s}(\mathbf{x})$ of Kriging using 15 observations; (b) $\hat{s}(\mathbf{x})$ by MLMC-based PhIK using 15 observations.

in Figure 15. For both methods, the error and uncertainty decrease with an increasing number of observations. Also, there are significant differences in the results. In Kriging, most new points are added near the boundary, while in MLMC-based PhIK, new measurements are added inside the domain close to the plume center. This is because the error in Kriging is dominated by the extrapolation error at the boundary. In MLMC-based PhIK, the boundary conditions in the physical model provide sufficient information near the boundaries. Consequently, the active learning algorithm explores more information around the plume. Moreover, compared with the first numerical example, the Gaussian kernel used in the Kriging method is less suitable for approximating the inhomogeneous field \mathbf{F} in this example. As a result, PhIK achieves higher accuracy than Kriging with a smaller number of observations. Finally, as an example of preserving linear constraints, the Dirichlet boundary on the left side is kept very well with maximum number smaller than $1e-6$.

4 Conclusion

In this work, we propose the PhIK method, where the mean and covariance function in the GP model are computed from a partially known physical model of the states. We also propose a novel MLMC estimate of the covariance function that, in combination with the standard MLMC estimate of the mean, leads to significant cost reduction in estimating statistics compared to the standard MC method. The resulting statistics in PhIK is non-stationary as can be expected for states of many physical systems due to their intrinsic inhomogeneity. This is different from the standard “data-driven” Kriging, where the mean and kernel are estimated from data only and usually requires an assumption of stationarity. In addition, PhIK avoids the need for estimating hyperparameters in the covariance function, which can be a challenging optimization problem.

We prove that PhIK preserves the physical knowledge if it is in the form of a deterministic linear operator. We also provide an upper error bound in the PhIK prediction in the presence of numerical errors. These theoretical results indicate that the accuracy of PhIK prediction depends on the physical model’s accuracy ($\|\mathbf{y} - \boldsymbol{\mu}\|_2$), numerical error (ϵ) the physical model’s stochastic properties, and the selection of observation locations ($(\|\mathbf{C} + \alpha\mathbf{I}\|_2)^{-1}$). We demonstrate that an active learning algorithm in combination with PhIK suggests very different locations for new observations than the data-driven Kriging and has the potential to result in significantly more accurate predictions with reduced uncertainty using fewer measurements. Other Kriging methods, e.g., university Kriging, may perform better than ordinary Kriging. However, such methods require non-stationary mean or kernel with larger numbers of hyperparameters, which adds to the difficulty of the optimization problem in identifying these hyperparameters.

Our method allows model and data convergence without solving complex optimization problems. Moreover, this method is nonintrusive as it can utilize existing domain codes to compute mean and covariance functions for GPR. This differs from other “physics-informed” GPR methods, e.g., [23, 55, 49, 50], where

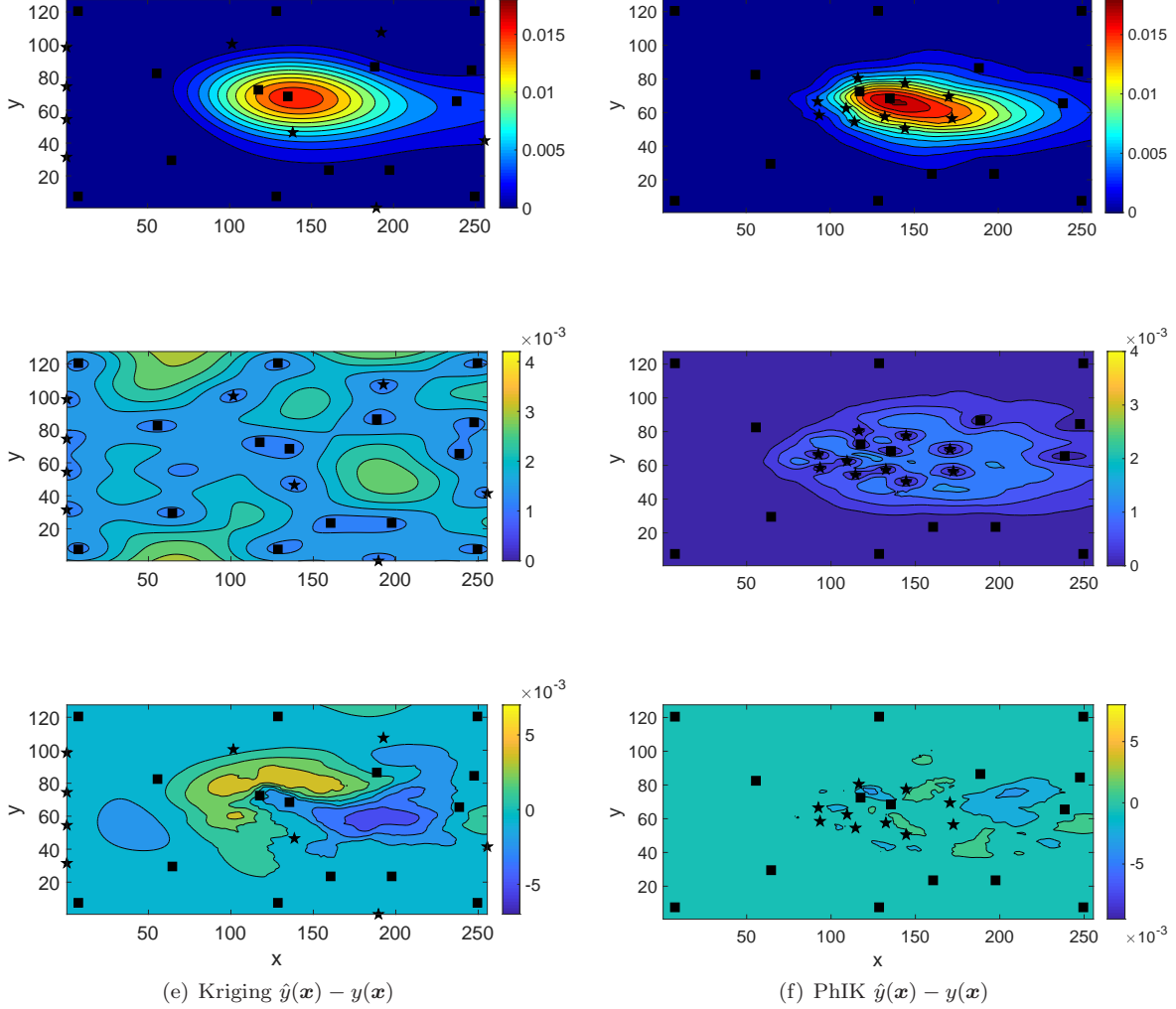


Figure 14: Solute transport: reconstruction of the solute concentration by Kriging and MLMC-based PhIK via active learning. Black squares mark the locations of the original eight observations, and stars are newly added observations. Left column: Kriging; right column: PhIK. First row: $\hat{y}(\mathbf{x})$; second row: $\hat{s}(\mathbf{x})$; third row: $\hat{y}(\mathbf{x}) - y(\mathbf{x})$.

physical laws are used to derive equations for the covariance function, which, in general, must be solved numerically. PhIK is especially suitable for problems with very costly observations and partially known physics models, including climate, oceanography, and transport in porous media. Such applications are governed by conservation laws, but the parameters, source/sink terms, and stresses in these conservation laws are often unknown and could be modeled as random processes.

Finally, it is worth repeating that the accuracy of PhIK prediction depends on the accuracy of the stochastic physical model. In other words, the PhIK accuracy depends on the distance between the exact solution and the linear space spanned by the simulation ensemble. The accuracy may be improved by adding correction terms, e.g, [67] and the cost of simulations may be further reduced by using other multi-fidelity approaches [71].

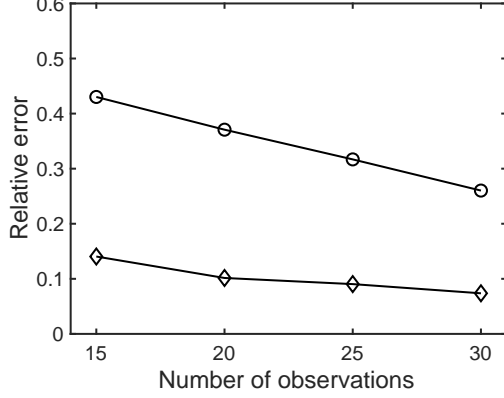


Figure 15: Solute transport: relative error of $\|\hat{y}(\mathbf{x}) - y(\mathbf{x})\|_2 / \|\hat{y}(\mathbf{x})\|_2$ of Kriging (“o”) and MLMC-based PhIK (“◊”) using different numbers of total observations via active learning.

Acknowledgments

This work was supported by the U.S. Department of Energy (DOE), Office of Science, Office of Advanced Scientific Computing Research (ASCR) as part of the Multifaceted Mathematics for Complex Systems and Uncertainty Quantification in Advection-Diffusion-Reaction Systems projects. A portion of the research described in this paper was conducted under the Laboratory Directed Research and Development Program at Pacific Northwest National Laboratory (PNNL). PNNL is operated by Battelle for the DOE under Contract DE-AC05-76RL01830.

A Proof of Theorems 2.1

Proof. The Kriging prediction Eq. (4) can be rewritten as the following function form:

$$\hat{y}(\mathbf{x}) = \mu(\mathbf{x}) + \sum_{i=1}^N a_i k(\mathbf{x}, \mathbf{x}^{(i)}), \quad (30)$$

where $\mathbf{x} \in D$, a_i is the i -th entry of $(\mathbf{C} + \alpha \mathbf{I})^{-1}(\mathbf{y} - \boldsymbol{\mu})$. Similarly, the PhIK prediction can be written as

$$\hat{y}(\mathbf{x}) = \mu_{MC}(\mathbf{x}) + \sum_{i=1}^N \tilde{a}_i k_{MC}(\mathbf{x}, \mathbf{x}^{(i)}), \quad (31)$$

where \tilde{a}_i is the i -th entry of $(\mathbf{C}_{MC} + \alpha \mathbf{I})^{-1}(\mathbf{y} - \boldsymbol{\mu}_{MC})$. We have

$$\begin{aligned} \|\mathcal{L}\mu_{MC}(\mathbf{x}) - \overline{g(\mathbf{x})}\| &= \left\| \frac{1}{M} \sum_{m=1}^M \mathcal{L}Y^m(\mathbf{x}) - \frac{1}{M} \sum_{m=1}^M g(\mathbf{x}; \omega^m) \right\| \\ &\leq \frac{1}{M} \sum_{m=1}^M \|\mathcal{L}Y^m(\mathbf{x}) - g(\mathbf{x}; \omega^m)\| \leq \epsilon. \end{aligned}$$

Also,

$$\begin{aligned}
& \|\mathcal{L}k_{MC}(\mathbf{x}, \mathbf{x}^{(i)})\| \\
&= \left\| \frac{1}{M-1} \sum_{m=1}^M \left(Y^m(\mathbf{x}^{(i)}) - \mu_{MC}(\mathbf{x}^{(i)}) \right) \mathcal{L} \left(Y^m(\mathbf{x}) - \mu_{MC}(\mathbf{x}) \right) \right\| \\
&\leq \frac{1}{M-1} \sum_{m=1}^M \left| Y^m(\mathbf{x}^{(i)}) - \mu_{MC}(\mathbf{x}^{(i)}) \right| \left\| \mathcal{L} \left(Y^m(\mathbf{x}) - \mu_{MC}(\mathbf{x}) \right) \right\| \\
&\leq \frac{1}{M-1} \sum_{m=1}^M \left| Y^m(\mathbf{x}^{(i)}) - \mu_{MC}(\mathbf{x}^{(i)}) \right| \cdot \\
&\quad \left\{ \left\| \mathcal{L}Y^m(\mathbf{x}) - g(\mathbf{x}; \omega^m) - \left(\mathcal{L}\mu_{MC}(\mathbf{x}) - \overline{g(\mathbf{x})} \right) \right\| + \|g(\mathbf{x}; \omega^m) - \overline{g(\mathbf{x})}\| \right\} \\
&\leq \frac{2\epsilon}{M-1} \left(M \sum_{m=1}^M \left| Y^m(\mathbf{x}^{(i)}) - \mu_{MC}(\mathbf{x}^{(i)}) \right|^2 \right)^{\frac{1}{2}} \\
&\quad + \frac{1}{M-1} \left(\sum_{m=1}^M \left| Y^m(\mathbf{x}^{(i)}) - \mu_{MC}(\mathbf{x}^{(i)}) \right|^2 \right)^{\frac{1}{2}} \left(\sum_{m=1}^M \|g(\mathbf{x}; \omega^m) - \overline{g(\mathbf{x})}\|^2 \right)^{\frac{1}{2}} \\
&= 2\epsilon \sqrt{\frac{M}{M-1}} \left(\frac{1}{M-1} \sum_{m=1}^M \left| Y^m(\mathbf{x}^{(i)}) - \mu_{MC}(\mathbf{x}^{(i)}) \right|^2 \right)^{\frac{1}{2}} \\
&\quad + \left(\frac{1}{M-1} \sum_{m=1}^M \left| Y^m(\mathbf{x}^{(i)}) - \mu_{MC}(\mathbf{x}^{(i)}) \right|^2 \right)^{\frac{1}{2}} \left(\frac{1}{M-1} \sum_{m=1}^M \|g(\mathbf{x}; \omega^m) - \overline{g(\mathbf{x})}\|^2 \right)^{\frac{1}{2}} \\
&= \left(2\epsilon \sqrt{\frac{M}{M-1}} + \sigma(g(\mathbf{x}; \omega^m)) \right) \sigma(Y^m(\mathbf{x}^{(i)})).
\end{aligned} \tag{32}$$

Thus, according to Eq. (31):

$$\begin{aligned}
\|\mathcal{L}\hat{y}(\mathbf{x}) - \overline{g(\mathbf{x})}\| &\leq \epsilon + \left[2\epsilon \sqrt{\frac{M}{M-1}} + \sigma(g(\mathbf{x}; \omega^m)) \right] \sum_{i=1}^N |\tilde{a}_i| \sigma(Y^m(\mathbf{x}^i)) \\
&\leq \epsilon + \left[2\epsilon \sqrt{\frac{M}{M-1}} + \sigma(g(\mathbf{x}; \omega^m)) \right] \max_{1 \leq i \leq N} |\tilde{a}_i| \sum_{i=1}^N \sigma(Y^m(\mathbf{x}^i))
\end{aligned}$$

Because $\max_i |\tilde{a}_i| = \|(\mathbf{C}_{MC} + \alpha \mathbf{I})^{-1}(\mathbf{y} - \boldsymbol{\mu}_{MC})\|_\infty$, the conclusion holds. \square

B Proof of Corollary 2.3

Proof.

$$\begin{aligned}
\|\mathcal{L}\bar{Y}^m(\mathbf{x})\| &= \|\mathcal{L}Y_H^m(\mathbf{x}) - \mathcal{L}Y_L^m(\mathbf{x})\| \\
&= \|\mathcal{L}Y_H^m(\mathbf{x}) - g(\mathbf{x}; \omega^m) - (\mathcal{L}Y_L^m(\mathbf{x}) - g(\mathbf{x}; \omega^m))\| \\
&\leq \epsilon_H + \epsilon_L.
\end{aligned}$$

We denote $\mu_L(\mathbf{x}) = \frac{1}{M_L} \sum_{m=1}^{M_L} Y_L^m(\mathbf{x})$, and $\bar{\mu}(\mathbf{x}) = \frac{1}{M_H} \sum_{m=1}^{M_H} \bar{Y}^m(\mathbf{x})$. According to Eq. (15), $\mu_{MLMC}(\mathbf{x}) = \mu_L(\mathbf{x}) + \bar{\mu}(\mathbf{x})$. By construction, $\|\mathcal{L}\mu_L(\mathbf{x}) - \overline{g(\mathbf{x})}\| \leq \epsilon_L$ and $\|\mathcal{L}\bar{\mu}(\mathbf{x})\| \leq \epsilon_L + \epsilon_H$. Thus,

$$\|\mathcal{L}\mu_{MLMC}(\mathbf{x}) - \overline{g(\mathbf{x})}\| = \left\| \mathcal{L}\mu_L(\mathbf{x}) - \overline{g(\mathbf{x})} + \mathcal{L}\bar{\mu}(\mathbf{x}) \right\| \leq 2\epsilon_L + \epsilon_H.$$

Following the same procedure in Eq. (32), we have

$$\begin{aligned} \left\| \frac{1}{M_L - 1} \sum_{m=1}^{M_L} \left(Y_L^m(\mathbf{x}^{(i)}) - \mu_L(\mathbf{x}^{(i)}) \right) \mathcal{L} \left(Y_L^m(\mathbf{x}) - \mu_L(\mathbf{x}) \right) \right\| \\ \leq \left(2\epsilon_L \sqrt{\frac{M_L}{M_L - 1}} + \sigma(g(\mathbf{x}; \omega^m)) \right) \sigma(Y_L^m(\mathbf{x}^{(i)})), \end{aligned}$$

and

$$\begin{aligned} \left\| \frac{1}{M_H - 1} \sum_{m=1}^{M_H} \left(\bar{Y}^m(\mathbf{x}^{(i)}) - \bar{\mu}(\mathbf{x}^{(i)}) \right) \mathcal{L} \left[\bar{Y}^m(\mathbf{x}) - \bar{\mu}(\mathbf{x}) \right] \right\| \\ \leq 2(\epsilon_H + \epsilon_L) \sqrt{\frac{M_H}{M_H - 1}} \sigma(\bar{Y}^m(\mathbf{x}^{(i)})). \end{aligned}$$

As such,

$$\begin{aligned} & \|\mathcal{L}\hat{y}(\mathbf{x}) - \overline{g(\mathbf{x})}\| \\ & \leq \epsilon_H + 2\epsilon_L + \left(2\epsilon_L \sqrt{\frac{M_L}{M_L - 1}} + \sigma(g(\mathbf{x}; \omega^m)) \right) \sum_{i=1}^N \tilde{a}_i \sigma(Y_L^m(\mathbf{x}^{(i)})) \\ & \quad + 2(\epsilon_H + \epsilon_L) \sum_{i=1}^N \tilde{a}_i \sqrt{\frac{M_H}{M_H - 1}} \sigma(\bar{Y}^m(\mathbf{x}^{(i)})) \\ & = \epsilon_H \left(1 + 2 \sum_{i=1}^N \tilde{a}_i \sqrt{\frac{M_H}{M_H - 1}} \sigma(\bar{Y}^m(\mathbf{x}^{(i)})) \right) \\ & \quad + \epsilon_L \left[2 + 2 \sum_{i=1}^N \tilde{a}_i \left(\sqrt{\frac{M_L}{M_L - 1}} \sigma(Y_L^m(\mathbf{x}^{(i)})) + \sqrt{\frac{M_H}{M_H - 1}} \sigma(\bar{Y}^m(\mathbf{x}^{(i)})) \right) \right] \\ & \quad + \sigma(g(\mathbf{x}; \omega^m)) \sum_{i=1}^N \tilde{a}_i \sigma(Y_L^m(\mathbf{x}^{(i)})). \end{aligned}$$

□

References

- [1] *Matlab partial differential equation toolbox*. <https://www.mathworks.com/products/pde.html>.
- [2] P. ABRAHAMSEN, *A review of Gaussian random fields and correlation functions*, 1997.
- [3] A. BARTH, C. SCHWAB, AND N. ZOLLINGER, *Multi-level Monte Carlo finite element method for elliptic PDEs with stochastic coefficients*, *Numerische Mathematik*, 119 (2011), pp. 123–161.
- [4] A. BERLINET AND C. THOMAS-AGNAN, *Reproducing kernel Hilbert spaces in probability and statistics*, Springer Science & Business Media, 2011.
- [5] C. BIERIG AND A. CHERNOV, *Convergence analysis of multilevel Monte Carlo variance estimators and application for random obstacle problems*, *Numerische Mathematik*, 130 (2015), pp. 579–613.
- [6] C. BIERIG AND A. CHERNOV, *Estimation of arbitrary order central statistical moments by the multilevel Monte Carlo method*, *Stochastics and Partial Differential Equations Analysis and Computations*, 4 (2016), pp. 3–40.

- [7] S. BRAHIM-BELHOUARI AND A. BERMAK, *Gaussian process for nonstationary time series prediction*, Computational Statistics & Data Analysis, 47 (2004), pp. 705–712.
- [8] K. A. CLIFFE, M. B. GILES, R. SCHEICHL, AND A. L. TECKENTRUP, *Multilevel Monte Carlo methods and applications to elliptic PDEs with random coefficients*, Computing and Visualization in Science, 14 (2011), p. 3.
- [9] D. A. COHN, Z. GHAMRANI, AND M. I. JORDAN, *Active learning with statistical models*, Journal of Artificial Intelligence Research, 4 (1996), pp. 129–145.
- [10] T. COLLET AND O. PIETQUIN, *Optimism in active learning with Gaussian processes*, in International Conference on Neural Information Processing, Springer, 2015, pp. 152–160.
- [11] C. CURRIN, T. MITCHELL, M. MORRIS, AND D. YLVIKAKER, *A bayesian approach to the design and analysis of computer experiments*, tech. report, Oak Ridge National Lab., TN (USA), 1988.
- [12] H. DAI, X. CHEN, M. YE, X. SONG, AND J. M. ZACHARA, *A geostatistics-informed hierarchical sensitivity analysis method for complex groundwater flow and transport modeling*, Water Resources Research, 53 (2017), pp. 4327–4343.
- [13] P. K. DAVIS AND J. H. BIGELOW, *Experiments in multiresolution modeling (mrm)*, tech. report, RAND CORP SANTA MONICA CA, 1998.
- [14] C. V. DEUTSCH AND A. G. JOURNEL, *GSLIB: Geostatistical Software Library and User’s Guide*, Oxford University Press, 1992.
- [15] C. R. DIETRICH AND G. N. NEWSAM, *Fast and exact simulation of stationary gaussian processes through circulant embedding of the covariance matrix*, SIAM Journal on Scientific Computing, 18 (1997), pp. 1088–1107.
- [16] N. DURRANDE, D. GINSBOURGER, AND O. ROUSTANT, *Additive covariance kernels for high-dimensional gaussian process modeling*, in Annales de la Faculté des sciences de Toulouse: Mathématiques, vol. 21, 2012, pp. 481–499.
- [17] S. EMMANUEL AND B. BERKOWITZ, *Mixing-induced precipitation and porosity evolution in porous media*, Advances in Water Resources, 28 (2005), pp. 337–344.
- [18] G. EVENSEN, *The ensemble Kalman filter: Theoretical formulation and practical implementation*, Ocean Dynamics, 53 (2003), pp. 343–367.
- [19] A. FORRESTER, A. KEANE, ET AL., *Engineering Design via Surrogate Modelling: A Practical Guide*, John Wiley & Sons, 2008.
- [20] G. GERACI, M. S. ELDRED, AND G. IACCARINO, *A multifidelity multilevel monte carlo method for uncertainty propagation in aerospace applications*, in 19th AIAA Non-Deterministic Approaches Conference, 2017, p. 1951.
- [21] M. GILES, *Improved multilevel Monte Carlo convergence using the Milstein scheme*, in Monte Carlo and quasi-Monte Carlo Methods 2006, Springer, 2008, pp. 343–358.
- [22] M. B. GILES, *Multilevel Monte Carlo path simulation*, Operations Research, 56 (2008), pp. 607–617.
- [23] P. HENNIG, M. A. OSBORNE, AND M. GIROLAMI, *Probabilistic numerics and uncertainty in computations*, Proceedings of the Royal Society London A, 471 (2015), p. 20150142.
- [24] S.-Y. HONG AND T. G. KIM, *Specification of multi-resolution modeling space for multi-resolution system simulation*, Simulation, 89 (2013), pp. 28–40.

- [25] Z. HOU, M. HUANG, L. R. LEUNG, G. LIN, AND D. M. RICCIUTO, *Sensitivity of surface flux simulations to hydrologic parameters based on an uncertainty quantification framework applied to the community land model*, Journal of Geophysical Research: Atmospheres, 117 (2012).
- [26] K. D. JARMAN AND A. M. TARTAKOVSKY, *A comparison of closures for stochastic advection-diffusion equations*, SIAM/ASA Journal on Uncertainty Quantification, 1 (2013), pp. 319–347.
- [27] D. R. JONES, M. SCHONLAU, AND W. J. WELCH, *Efficient global optimization of expensive black-box functions*, Journal of Global optimization, 13 (1998), pp. 455–492.
- [28] M. C. KENNEDY AND A. O’HAGAN, *Predicting the output from a complex computer code when fast approximations are available*, Biometrika, 87 (2000), pp. 1–13.
- [29] P. K. KITANIDIS, *Introduction to Geostatistics: Applications in Hydrogeology*, Cambridge University Press, 1997.
- [30] A. KRAUSE, A. SINGH, AND C. GUESTRIN, *Near-optimal sensor placements in Gaussian processes: Theory, efficient algorithms and empirical studies*, J. Mach. Learn. Res., 9 (2008), pp. 235–284.
- [31] G. LIN AND A. M. TARTAKOVSKY, *An efficient, high-order probabilistic collocation method on sparse grids for three-dimensional flow and solute transport in randomly heterogeneous porous media*, Advances in Water Resources, 32 (2009), pp. 712–722.
- [32] F. LINDGREN, H. RUE, AND J. LINDSTRÖM, *An explicit link between gaussian fields and gaussian markov random fields: the stochastic partial differential equation approach*, Journal of the Royal Statistical Society: Series B (Statistical Methodology), 73 (2011), pp. 423–498.
- [33] L. MARGHERI AND P. SAGAUT, *A hybrid anchored-ANOVA-POD/Kriging method for uncertainty quantification in unsteady high-fidelity CFD simulations*, Journal of Computational Physics, 324 (2016), pp. 137–173.
- [34] C. A. MICCHELLI AND G. WAHBA, *Design problems for optimal surface interpolation.*, tech. report, Wisconsin Univ-Madison Dept of Statistics, 1979.
- [35] J. M. MURPHY, D. M. SEXTON, D. N. BARNETT, G. S. JONES, M. J. WEBB, M. COLLINS, AND D. A. STAINFORTH, *Quantification of modelling uncertainties in a large ensemble of climate change simulations*, Nature, 430 (2004), p. 768.
- [36] L. W.-T. NG AND M. ELDRED, *Multifidelity uncertainty quantification using non-intrusive polynomial chaos and stochastic collocation*, in 53rd AIAA/ASME/ASCE/AHS/ASC Structures, Structural Dynamics and Materials Conference 20th AIAA/ASME/AHS Adaptive Structures Conference 14th AIAA, 2012, p. 1852.
- [37] H. NIEDERREITER, *Random Number Generation and Quasi-Monte Carlo Methods*, vol. 63, SIAM, 1992.
- [38] H. OWHADI, *Bayesian numerical homogenization*, Multiscale Modeling & Simulation, 13 (2015), pp. 812–828.
- [39] H. OWHADI, *Multigrid with rough coefficients and multiresolution operator decomposition from hierarchical information games*, SIAM Review, 59 (2017), pp. 99–149.
- [40] C. J. PACIOREK AND M. J. SCHERVISH, *Nonstationary covariance functions for Gaussian process regression*, in Advances in Neural Information Processing Systems, 2004, pp. 273–280.
- [41] L. PARUSSINI, D. VENTURI, P. PERDIKARIS, AND G. E. KARNIADAKIS, *Multi-fidelity gaussian process regression for prediction of random fields*, Journal of Computational Physics, 336 (2017), pp. 36–50.

- [42] B. PEHERSTORFER, K. WILLCOX, AND M. GUNZBURGER, *Survey of multifidelity methods in uncertainty propagation, inference, and optimization*, Siam Review, 60 (2018), pp. 550–591.
- [43] P. PERDIKARIS, D. VENTURI, AND G. E. KARNIADAKIS, *Multifidelity information fusion algorithms for high-dimensional systems and massive data sets*, SIAM Journal on Scientific Computing, 38 (2016), pp. B521–B538.
- [44] P. PERDIKARIS, D. VENTURI, J. O. ROYSET, AND G. E. KARNIADAKIS, *Multi-fidelity modelling via recursive co-kriging and gaussian–markov random fields*, Proceedings of the Royal Society A: Mathematical, Physical and Engineering Sciences, 471 (2015), p. 20150018.
- [45] C. PLAGEMANN, K. KERSTING, AND W. BURGARD, *Nonstationary Gaussian process regression using point estimates of local smoothness*, in Joint European Conference on Machine Learning and Knowledge Discovery in Databases, Springer, 2008, pp. 204–219.
- [46] Y. QIAN, C. JACKSON, F. GIORGI, B. BOOTH, Q. DUAN, C. FOREST, D. HIGDON, Z. J. HOU, AND G. HUERTA, *Uncertainty quantification in climate modeling and projection*, Bulletin of the American Meteorological Society, 97 (2016), pp. 821–824.
- [47] J. QUINONERO-CANDELA AND C. E. RASMUSSEN, *A unifying view of sparse approximate gaussian process regression*, The Journal of Machine Learning Research, 6 (2005), pp. 1939–1959.
- [48] L. RABELO, K. KIM, T. W. PARK, J. PASTRANA, M. MARIN, G. LEE, K. NAGADI, B. IBRAHIM, AND E. GUTIERREZ, *Multi resolution modeling*, in Proceedings of the 2015 Winter Simulation Conference, WSC '15, IEEE Press, 2015, pp. 2523–2534.
- [49] M. RAISSI, P. PERDIKARIS, AND G. E. KARNIADAKIS, *Machine learning of linear differential equations using Gaussian processes*, Journal of Computational Physics, 348 (2017), pp. 683–693.
- [50] M. RAISSI, P. PERDIKARIS, AND G. E. KARNIADAKIS, *Numerical Gaussian processes for time-dependent and nonlinear partial differential equations*, SIAM Journal on Scientific Computing, 40 (2018), pp. A172–A198.
- [51] C. E. RASMUSSEN, *Gaussian processes in machine learning*, in Advanced Lectures on Machine Learning, Springer, 2004, pp. 63–71.
- [52] C. E. RASMUSSEN AND H. NICKISCH, *Gaussian processes for machine learning (gpml) toolbox*, The Journal of Machine Learning Research, 11 (2010), pp. 3011–3015.
- [53] K. RITTER, *Average-case Analysis of Numerical Problems*, Springer, 2007.
- [54] J. SACKS, W. J. WELCH, T. J. MITCHELL, AND H. P. WYNN, *Design and analysis of computer experiments*, Statistical Science, (1989), pp. 409–423.
- [55] M. SCHÖBER, D. K. DUVENAUD, AND P. HENNIG, *Probabilistic ODE solvers with Runge-Kutta means*, in Advances in Neural Information Processing Systems, 2014, pp. 739–747.
- [56] M. L. STEIN, *Interpolation of Spatial Data: Some Theory for Kriging*, Springer Science & Business Media, 2012.
- [57] A. M. TARTAKOVSKY, S. P. NEUMAN, AND R. J. LENHARD, *Immiscible front evolution in randomly heterogeneous porous media*, Physics of Fluids (1994-present), 15 (2003), pp. 3331–3341.
- [58] A. M. TARTAKOVSKY, M. PANZERI, G. D. TARTAKOVSKY, AND A. GUADAGNINI, *Uncertainty quantification in scale-dependent models of flow in porous media*, Water Resources Research, 53 (2017), pp. 9392–9401.

- [59] S. TONG AND D. KOLLER, *Support vector machine active learning with applications to text classification*, Journal of Machine Learning Research, 2 (2001), pp. 45–66.
- [60] M. D. WHITE AND M. OOSTROM, *STOMP subsurface transport over multiple phases, version 4.0, user’s guide*, tech. report, PNNL-15782, Richland, WA, 2006.
- [61] C. K. WILLIAMS AND C. E. RASMUSSEN, *Gaussian processes for machine learning*, the MIT Press, 2 (2006), p. 4.
- [62] C. K. WILLIAMS AND F. VIVARELLI, *Upper and lower bounds on the learning curve for Gaussian processes*, Machine Learning, 40 (2000), pp. 77–102.
- [63] J. WITTEVEEN, K. DURAISAMY, AND G. IACCARINO, *Uncertainty quantification and error estimation in scramjet simulation*, in 17th AIAA International Space Planes and Hypersonic Systems and Technologies Conference, 2011, p. 2283.
- [64] N.-C. XIAO, M. J. ZUO, AND C. ZHOU, *A new adaptive sequential sampling method to construct surrogate models for efficient reliability analysis*, Reliability Engineering & System Safety, 169 (2018), pp. 330–338.
- [65] D. XIU AND J. S. HESTHAVEN, *High-order collocation methods for differential equations with random inputs*, SIAM Journal on Scientific Computing, 27 (2005), pp. 1118–1139.
- [66] B. YANG, Y. QIAN, G. LIN, L. R. LEUNG, P. J. RASCH, G. J. ZHANG, S. A. MCFARLANE, C. ZHAO, Y. ZHANG, H. WANG, ET AL., *Uncertainty quantification and parameter tuning in the cam5 zhang-mcfarlane convection scheme and impact of improved convection on the global circulation and climate*, Journal of Geophysical Research: Atmospheres, 118 (2013), pp. 395–415.
- [67] X. YANG, D. BARAJAS-SOLANO, G. TARTAKOVSKY, AND A. M. TARTAKOVSKY, *Physics-informed cokriging: A gaussian-process-regression-based multifidelity method for data-model convergence*, Journal of Computational Physics, 395 (2019), pp. 410–431.
- [68] X. YANG, M. CHOI, G. LIN, AND G. E. KARNIADAKIS, *Adaptive ANOVA decomposition of stochastic incompressible and compressible flows*, Journal of Computational Physics, 231 (2012), pp. 1587–1614.
- [69] X. YANG AND G. E. KARNIADAKIS, *Reweighted ℓ_1 minimization method for stochastic elliptic differential equations*, Journal of Computational Physics, 248 (2013), pp. 87–108.
- [70] X. YANG, D. VENTURI, C. CHEN, C. CHRYSOSTOMIDIS, AND G. E. KARNIADAKIS, *EOF-based constrained sensor placement and field reconstruction from noisy ocean measurements: Application to Nantucket Sound*, Journal of Geophysical Research: Oceans, 115 (2010), p. C12072.
- [71] X. YANG, X. ZHU, AND J. LI, *When bifidelity meets cokriging: An efficient physics-informed multifidelity method*, SIAM Journal on Scientific Computing, 42 (2020), pp. A220–A249.
- [72] D. YLVIKAKER, *Designs on random fields*, A Survey of Statistical Design and Linear Models, 37 (1975), pp. 593–607.
- [73] M. YUAN, T. T. CAI, ET AL., *A reproducing kernel hilbert space approach to functional linear regression*, The Annals of Statistics, 38 (2010), pp. 3412–3444.
- [74] Y. ZHANG AND J. G. BELLINGHAM, *An efficient method of selecting ocean observing locations for capturing the leading modes and reconstructing the full field*, Journal of Geophysical Research: Oceans, 113 (2008), p. C04005.
- [75] Z. ZHANG, X. YANG, I. V. OSELEDETS, G. E. KARNIADAKIS, AND L. DANIEL, *Enabling high-dimensional hierarchical uncertainty quantification by anova and tensor-train decomposition*, IEEE Transactions on Computer-Aided Design of Integrated Circuits and Systems, 34 (2014), pp. 63–76.

- [76] X. ZHU, E. M. LINEBARGER, AND D. XIU, *Multi-fidelity stochastic collocation method for computation of statistical moments*, *Journal of Computational Physics*, 341 (2017), pp. 386–396.